SEDIMENTOLOGY the journal of the International Association of Sedimentologists

Sedimentology (2011) **58,** 1573–1612 doi: 10.1111/j.1365-3091.2011.01226.x

Deposit architecture and dynamics of the 2006 block-and-ash flows of Merapi Volcano, Java, Indonesia

SYLVAIN J. CHARBONNIER[1] and RALF GERTISSER
School of Physical and Geographical Sciences, Earth Sciences and Geography, Keele University, Keele, Staffordshire ST5 5BG, UK (E-mail: sylvain@usf.edu)

Associate Editor – Vern Manville

ABSTRACT

The internal architecture of the 2006 block-and-ash flow deposits of Merapi volcano (Java, Indonesia) was investigated using data collected from 27 stratigraphic sections measured immediately after flow emplacement, and after one and two rainy seasons of erosion. Identification of different depositional units and their longitudinal and lateral facies variations provide detailed information about: (i) the distribution, volumes and sedimentological characteristics of the different units; (ii) flow types and mobility as inferred from associated deposits; and (iii) changes in the dynamics of the different flows and their material during emplacement. Two main types of block-and-ash flows (short-runout to medium-runout block-and-ash flows and long-runout block-and-ash flows) are defined based on flow generation mechanism, flow volume, travel distance, deposit morphology, distribution, lithology and grain-size distribution. Conceptual models for the transport and depositional mechanisms of these two types of block-and-ash flows are presented. Variations in the runout distances observed for short-runout to medium-runout block-and-ash flows are linked directly to different initial flow volumes, degree of fragmentation and material properties of the moving mass during transport, with the largest and finer grained flows having the greatest mobility. Deposition occurs only over a narrow range of basal inclinations close to the angle of repose for pyroclastic material, indicating that such flows behave in a similar way to granular-free surface flows on unconfined planes. The flow mechanisms of long-runout block-and-ash flows at Merapi are interpreted to be similar, in many respects, to unsteady, cohesionless grain flows with an inertial flow regime where collisional forces largely overcome frictional forces. Flow unsteadiness causes the main body to be segmented into different pulses that run closer to each other as the flow moves downslope. Deposition occurs stepwise, with rapid aggradation of stacked sub-units from different parts of the major flow pulses. In such a model, the arrival of each flow pulse front at selected sites in the main river valley controls the generation and development of highly mobile, unconfined pyroclastic flows outside valley regions and their associated overbank deposits.

Keywords Sedimentology, block-and-ash flows, Merapi volcano, flow parameters, emplacement mechanisms.

[1]Present address: Department of Geology, University of South Florida, Tampa, Florida 33620-5201, USA.

INTRODUCTION

In recent years, significant advances in understanding of the dynamics of small-volume pyroclastic flows have been made through sedimentological and geophysical investigations (e.g. Druitt, 1998; Branney & Kokelaar, 2002; Sulpizio & Dellino, 2008), laboratory experiments (e.g. Roche *et al.*, 2004; Lube *et al.*, 2005; Dellino *et al.*, 2007) and numerical simulations (e.g. Patra *et al.*, 2005; Doyle *et al.*, 2010). Block-and-ash flows (BAFs) are pyroclastic flows that are generated by the gravitational or explosive collapse of viscous lava domes and characterized by complex, gravity-controlled, multi-phase flow dynamics (e.g. Branney & Kokelaar, 2002; Sulpizio & Dellino, 2008). The deposits of BAFs generally consist of poorly sorted mixtures of decimetre to metre-sized, dense to moderately vesicular blocks set within a coarse ash matrix (e.g. Cas & Wright, 1987; Druitt, 1998). Particle organization in granular flows due to particle collisions, stress transfer and gravitational forces (e.g. Bagnold, 1954; Savage, 1979; Takahashi, 1981) are currently the most favoured processes to explain many of the key sedimentary features observed in BAF deposits. The BAF system differs slightly in that component particles are hot, with at times high internal pore pressures, leading to rapid particle disintegration (e.g. Ritchie *et al.*, 2002). The BAFs are topographically controlled and typically comprise two components, a high-density ground-hugging basal avalanche component, in which the bulk of material is transported, and an overriding, dilute ash cloud (e.g. Cas & Wright, 1987; Druitt, 1998; Branney & Kokelaar, 2002; Sulpizio & Dellino, 2008). Due to the predominantly coarse-grained and cohesionless nature of their basal component, gas release on fragmentation is not thought to significantly modify the granular flow behaviour (e.g. Hayashi & Self, 1992). However, BAFs are particularly complex as it is difficult to predict the scale, duration, periodicity and spatial distribution of the flows. This is partly due to the characteristics of the source lava dome itself (for example, size, volume, orientation and material rheology), but also to the nature and complexity of the topographic profile of the volcanoes both near the dome (proximal areas) and down the flanks (medial to distal areas). Traditionally, qualitative techniques for studying BAFs have been crucial to improve knowledge of their transport and depositional processes. Descriptions of BAFs and their deposits, often combined with conceptual models of generation and emplacement mechanisms, are available from other volcanoes around the world, including Colima (e.g. Saucedo *et al.*, 2002, 2004), Unzen (e.g. Miyabuchi, 1999) and Ngauruhoe (Lube *et al.*, 2007), as well as from some recent Merapi eruptions (Boudon *et al.*, 1993; Abdurachman *et al.*, 2000; Schwarzkopf *et al.*, 2005; Charbonnier & Gertisser, 2008; Gomez *et al.*, 2009).

During the May to June 2006 eruptive episode of Merapi, BAFs affected densely populated areas on the southern flank of the volcano and were the first major flows in the area surrounding the Gendol river valley for over a century (Fig. 1). The flows were not confined to the existing river valleys but spilled over the valley sides to create overbank (unconfined) pyroclastic flows that resulted in fatalities and destruction in the village of Kaliadem (Charbonnier & Gertisser, 2008). From the local stratigraphic record, it can be inferred that the 2006 events were only some of the latest in a number of explosive eruptions affecting the area around Kaliadem and the southern flank of Merapi. More recently, the 2010 eruptive activity has confirmed these observations when, on 26 October 2010, an eruption began that was characterized by explosions along with unconfined pyroclastic flows that travelled to the western and southern sectors of the volcano. Reports from the Center of Volcanology and Geological Hazard Mitigation (CVGHM) showed that explosive activity increased during the following days until 4 and 5 November 2010, when a series of large explosions sent various pyroclastic flows and surges *ca* 15 km away from the summit mainly directed towards the southern sector, filling several valleys, spreading across the interfluves and killing more than 300 people (source: CVGHM). The occurrence of substantial interfluve deposits suggests that the generation of unconfined pyroclastic flows that escape the valley confines is a common process at Merapi. In this respect, the present paper investigates the dynamics of small-volume pyroclastic flows through an extensive study of the 2006 BAFs of Merapi. It consists of three parts: (i) a stratigraphical and granulometrical study of the June 2006 BAFs based on 27 stratigraphic sections measured along the deposits; (ii) an investigation of lateral and vertical facies variations of the deposits; and (iii) an analysis of the distribution, volumes and sedimentological characteristics of the different units. The results from this study combined with published data from other types of pyroclastic density currents provide valuable information

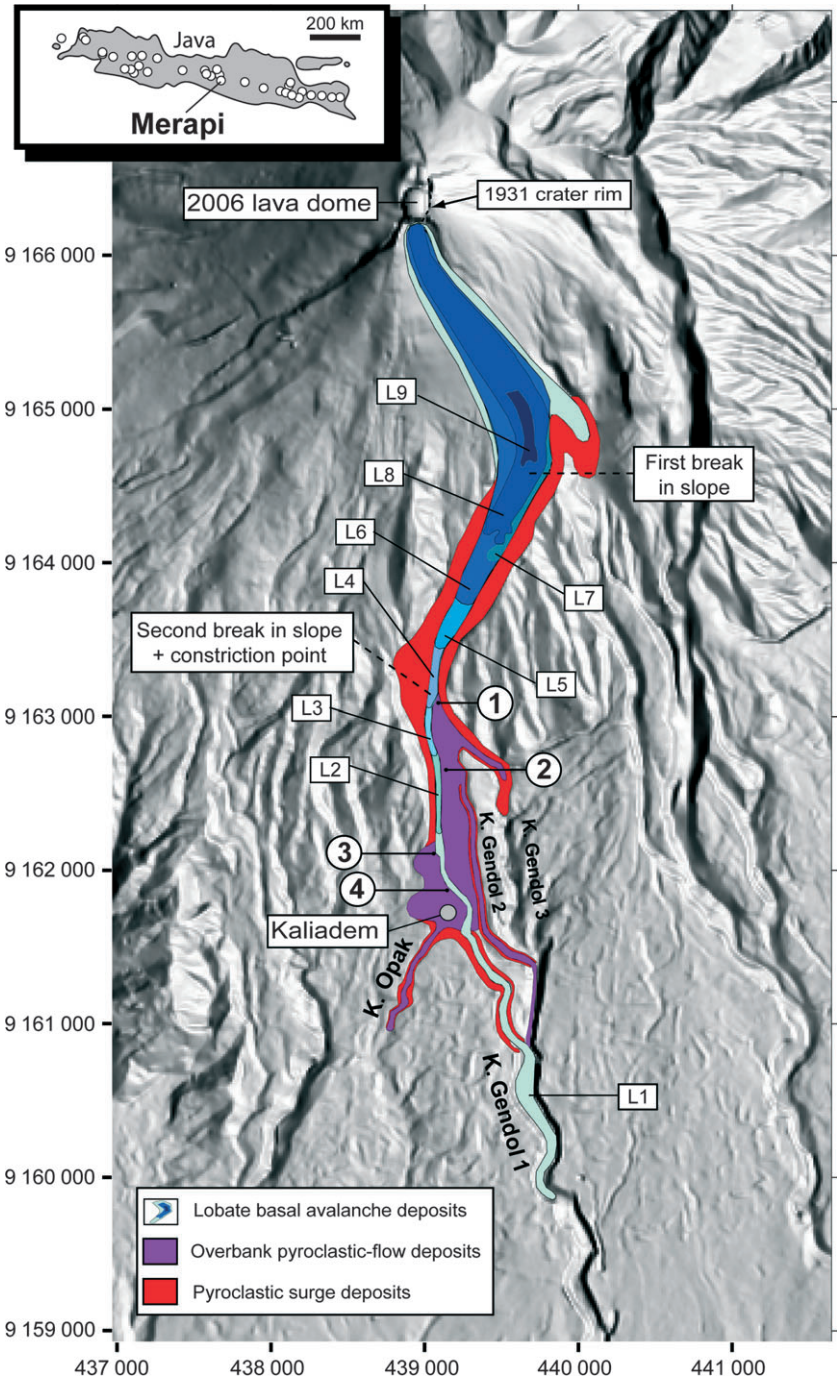

Fig. 1. Geological map of the June 2006 block-and-ash flow (BAF) deposits that fill the Gendol river valley [Kali (K.) Gendol] and adjacent areas on the southern flank of Merapi (after Charbonnier & Gertisser, 2008), superimposed onto a digital elevation model (courtesy of C. Gerstenecker, Technische Universität Darmstadt, Germany). The BAF deposits generated during (and after) the peak of the eruptive activity on 14 June 2006 are shown as individual, overlapping lobes ('L1' to 'L9'). Numbers ('1' to '4') correspond to the key sites where the 14 June p.m. BAF (L1) overspilled the confines of the channel. The coordinates are in UTM metres. The inset map shows the location of Merapi and other active volcanoes (open circles) in Java, Indonesia.

about the types and mobility of the June 2006 BAFs that help to improve models of BAF dynamics and related hazards.

THE 2006 ERUPTION OF MERAPI VOLCANO

After five years of repose, volcanic activity at Merapi resumed in July 2005 with an increase in the number of volcanic earthquakes and deformation of the summit area. This renewed episode of unrest ended with the extrusion of a new lava dome on 28 April 2006 (BGVN, 2007). Due to the particular location of the active lava dome, and the presence of a topographic barrier to the south of the new dome, the rockfalls and BAFs of May 2006 were directed mainly towards the southwestern flank of Merapi with runout distances of typically less than 4 km (i.e. into the Krasak,

Bedok and Boyong river valleys – BGVN 2007; Charbonnier & Gertisser, 2008). Towards the end of May 2006, the daily number of rockfalls and pyroclastic flows increased gradually. After a tectonic earthquake on 27 May, located *ca* 35 km south of Merapi near the village of Bantul, a significant increase in the magma extrusion rate and associated dome collapse events occurred (BGVN, 2007; Walter *et al.*, 2007). In June 2006, the main pyroclastic flow activity shifted to the southern and south-eastern flanks of Merapi, with flows entering the upper Woro drainage and, predominantly, the Gendol river valley (BGVN 2007; Charbonnier & Gertisser, 2008). Most of the flows in early June extended less than 5 km from the source. On 14 June, the activity peaked with two sustained dome-collapse events that generated BAFs with runout distances of 5 km (14 June a.m. flow) and 7 km (14 June p.m. flow), respectively. The largest of these events (14 June p.m. flow) caused two fatalities and partial burial of the village of Kaliadem some 5 km from the summit (Fig. 1). After 14 June, both the number of dome collapse events and the extent of pyroclastic flows decreased throughout the second half of June. The activity of Merapi dropped to background levels in early July 2006 (BGVN 2007).

The deposits of the eruption were examined immediately after flow emplacement to unravel the relationship between individual flow deposits and the documented eruption record (Charbonnier & Gertisser, 2008). These deposits form at least nine overlapping lobes, which represent a record of flows generated during and after the major dome-collapse event of 14 June (Charbonnier & Gertisser, 2008). The 2006 deposits comprise: (i) valley-confined basal avalanche deposits in the main river valley (K. Gendol 1; K = Kali which means river in Indonesian; (ii) overbank pyroclastic-flow deposits, where parts of the basal avalanche spread laterally onto interfluves at several sites along the main channel and subsequently were re-channelled into the surrounding river valleys; and (iii) dilute ash-cloud surge deposits along the valley margins. Variations in the distribution, surface morphology and lithology of the deposits are related to the source materials involved during individual pyroclastic-flow forming events and to the effects of changing slope, channel morphology and local topographic features on the flow dynamics. In the proximal area (<4·5 km from the summit), individual flows form eight, small-volume lobate deposits with steep, bouldery and clast-supported fronts (L2 to L9, Fig. 1) that overlie the basal avalanche deposits of the 14 June p.m. flow (L1, Fig. 1). All flow units are massive mixtures of decimetre-sized to metre-sized blocks set within a matrix of fine-lapilli to medium-ash grade. The BAF deposits emplaced on 14 June emphasize the potential hazard of voluminous BAFs at Merapi through the generation of overbank pyroclastic flows. Field observations (Charbonnier & Gertisser, 2008) suggest that, during the eruption, the basal avalanche of the 14 June p.m. flow was able to spill over the valley sides in four locations (Fig. 1).

METHODS AND TERMINOLOGY

Data collection

Two field campaigns carried out in 2007 and 2008 offered the opportunity to perform a detailed study of the sedimentological, stratigraphical, granulometrical and componentry characteristics of the different deposits after the first and second rainy seasons following the eruption. From the measured stratigraphic sections along the June 2006 BAF deposits, 42 samples from different units were collected, with the aim of including all three types of deposits mapped during the 2006 survey.

The distribution of the collected samples along the flow paths was controlled strongly by the distribution and availability of erosive channels and primary deposits. A study of the deposit surface revealed significant differences between deposits from channelled, valley-confined basal avalanches and overbank pyroclastic flows (Charbonnier & Gertisser, 2008). Lithofacies analysis has previously been applied to investigate lateral and vertical variations of sedimentary structures within complex sequences of small-volume pyroclastic-flow deposits and ignimbrites (e.g. Freundt & Schmincke, 1986; Sohn & Chough, 1989; Druitt, 1992; Cole *et al.*, 1993; Allen & Cas, 1998; Sulpizio *et al.*, 2007). Field-based studies of BAFs at Merapi (Boudon *et al.*, 1993; Abdurachman *et al.*, 2000; Kelfoun *et al.*, 2000; Bourdier & Abdurachman, 2001; Schwarzkopf *et al.*, 2005) have distinguished: (i) valley-filling deposits that are primarily a result of channel confinement, slope effects and pre-event and syn-event topography; and (ii) deposits outside valley confines (i.e. overbank deposits) that are generated by the breakout of channelled BAFs onto interfluve regions or by ash-cloud surges derived and

Table 1. Lithofacies scheme for the June 2006 block-and-ash flow (BAF) deposits of Merapi.

BAF component	Facies	Description	Interpretation	Reference
Basal avalanche	Massive Blocks, Lapilli and Ash with strong clast segregation (mBLAss)	Thickness >1 m Poorly sorted with blocks set in a lapilli–ash matrix Strong coarse-tail inverse grading and coarse-clast free basal zone Clast trains and grain fabric orientations are common, with long axes of elongated clasts mostly parallel to the flow direction {[a(p),b(i)]} Erosional basal contacts and striations on substrate are frequent	Frozen state of part of a quasi-steady to unsteady granular pyroclastic density current in which grain interactions and fragmentation processes developed a sufficient granular temperature to induce segregation processes such as kinetic sieving (Middleton, 1970; Savage & Lun, 1988) and kinematic squeezing (Le Roux, 2003) of the largest particles Rapid freezing of the basal flow portion and high shear stresses in a frictional regime occur at the time of deposition	Unit L4 at section CS4 (Fig. 2) Unit L1A at sections CS1, CS5, CS6 and CS9 (Figs 2 and 3) Unit L1M at sections CS5 and CS6 (Figs 2 and 3) Unit OB2 at sections IN2, IN3, IN4 and KG1 (Fig. 5) Unit OB1 at sections IN1 and KA2 (Fig. 5)
	Massive Blocks, Lapilli and Ash with moderate clast segregation (mBLAms)	Thickness up to 15 m Poorly sorted with blocks set in a lapilli–ash matrix. Maximum range of grain size distribution Massive with weak or absent coarse-tail grading and coarse-clast free basal zone Rare clast trains and moderate grain fabric orientation with long axes of elongated clasts oriented mostly flow-parallel {[a(p),b(i)]} or flow-perpendicular {[a(t),b(i)]} Rare erosional basal contacts	Frozen state of the main body of a quasi-steady to unsteady granular pyroclastic density current in which grain interactions and fragmentation processes are more subdued but sufficient to induce moderate segregation processes such as kinetic sieving and kinematic squeezing of the largest particles Rapid and massive freezing occurs at the time of deposition	Unit L6 at section CS1 (Fig. 2) Unit L3 at section CS4 (Fig. 2) Unit L2 at section CS5 (Fig. 2) Unit L1A at sections CS11, CS14 and CS16 (Figs 3 and 4) Unit L1M at section CS7 (Fig. 3) Unit OB2 at sections KA1 and KG2 (Fig. 5) Unit OB1 at sections IN2, IN3, KA1 and KA3 (Fig. 5)

Table 1. (*Continued*)

BAF component	Facies	Description	Interpretation	Reference
	Massive Blocks, Lapilli and Ash or Massive Lapilli and Ash with weak clast segregation (mBLAws, mLAws)	Thickness >1 m Poorly sorted with blocks set in a lapilli–ash matrix Massive with weak coarse-tail normal grading and no coarse-clast free basal zone Rare clast trains and minor or absent grain fabric orientation Almost universal preservation of underlying fragile substrates	Frozen state of part of a quasi-steady to unsteady granular pyroclastic density current in which kinetic energy and grain dispersive pressure dropped Loss of momentum and competence of the flow with high shear stresses in a frictional regime when the flow becomes to rest	Unit L6 at section CS2 (Fig. 2) Unit L5 at section CS3 (Fig. 2) Unit L2 at section CS7 (Fig. 2) Unit L1A at section CS17 (Fig. 4) Unit L1M at section CS9 (Fig. 3) Unit OB2 at sections KA2 and KG3 (Fig. 5)
Ash-cloud surge	Massive Lapilli and Ash or Massive Ash (mLA, mA)	Thickness <20 cm and almost constant at the scale of the outcrop Moderately to well-sorted lapilli–ash or ash layer with frequent unimodal grain-size distribution Massive or weak coarse-tail normal grading. No stratification Usually found in association with mBLAss or mBLAms	Gentle settling of an ash-cloud surge accompanying a quasi-steady to unsteady granular pyroclastic density current. Could also be emplaced by the lofting and entrapment of fine ash produced during the passage of such a current at a break in slope	Unit S3 at section CS4 (Fig. 2) Unit S1A at sections CS1, CS2, CS5 and CS7 (Figs 2 and 3) Unit S1M at section CS5 (Fig. 2) Unit S1 at sections IN3 and KA2 (Fig. 5)

separated from the channelled flows. Using deposit componentry, sedimentary structures, grain size and sorting, six main lithofacies are distinguished here to describe the internal architecture of the June 2006 deposits in terms of the grain size and granular segregation structures (coarse-tail grading, clast train and grain fabric orientation) of the deposits: mBLAss (Massive Blocks, Lapilli and Ash with strong clast segregation); mBLAms (Massive Blocks, Lapilli and Ash with moderate clast segregation); mBLAws (Massive Blocks, Lapilli and Ash with weak clast segregation); mLAws (Massive Lapilli and Ash with weak clast segregation); mLA (Massive Lapilli and Ash); and mA (Massive Ash) (Table 1).

Accordingly, 28 samples from 17 stratigraphic sections located inside the major gullies were collected from the valley-filling deposits of the June 2006 BAFs. Ten sections (14 samples) situated on the interfluves and the surrounding valleys correspond to the overbank deposits of these flows. The terms 'depositional unit' or 'flow unit', as used in this paper, refer to a single pyroclastic flow deposited in one lobe. When several flow units pile up rapidly, one on top of the other, they may cool as a single 'cooling unit' (Fisher & Schmincke, 1984). Here, the term 'unit' has been used to avoid any genetic implication and refers to a deposit bound by erosive or gradational contacts (for example, soil, ash or surge layer, trains of blocks and/or grain-size breaks). Stratigraphic units of the valley-filling deposits are named 'L' and their numbers are correlated with previously identified lobe deposits at the surface (for example, unit L1 for lobe 1), as described in detail in Charbonnier (2009). Exposed units of the overbank deposits are labelled 'OB' and the term 'S' is used for those of the associated ash-cloud surge deposits. The nomenclature for bed (unit) thickness, grain size and sorting is adapted from Sohn & Chough (1989) and follows that of Sulpizio *et al.* (2007).

Grain-size analysis

Grain-size analysis of the bulk June 2006 BAF deposits is made difficult by the extremes in block sizes usually present, with >2 m diameter blocks in a <32 μm diameter fine-ash matrix at some locations. Therefore, a multiple-step method was carried out to analyse the grain-size distributions of the collected samples. Depending on the local thickness and the internal structure, the different stratigraphic units were subdivided into two or three zones in which scaled rectangular areas of about $0{\cdot}5 \times 1{\cdot}5$ m were sampled. Large particles at the margin of the sampled area were collected with the sample when protruding more than 50% into the sample box. For each sample, all bulk material was extracted and weighed in the field with a field scale. The grain-size distribution for the fractions from −6 phi (64 mm) to −2 phi (4 mm) was determined by gentle dry sieving in full phi intervals in the field. Subsequently, due to the large remaining mass (>10 kg) of the fractions smaller than −2 phi, only a quarter of the total mass (*ca* 3 kg) was kept to carry out wet-sieving in the laboratory at 1 phi intervals, down to 5 phi (32 μm). Following the work of Schumacher *et al.* (1990) on soil sample homogenization, the cone and quarter method was used in the field and the riffle splitting method (using closed bins) in the laboratory in order to obtain similar distributions of the fractions smaller than −2 phi into each subsample during splitting. The original samples were sieved twice to test the replicate variability of the method and results suggest uncertainties <15% on a single grain size and <5% on the total grain-size distribution of the samples tested. Fractions smaller than 5 phi were not integrated into the grain-size distributions to facilitate comparison between samples. However, estimates based on the loss of fines during sieving showed that their mass never exceeded 10 wt% of the total sample mass. Additionally, deposit photographs of the sample boxes were analysed using the 'UTHSCSA ImageTool 3.00' software (developed at the University of Texas Health Science Center at San Antonio, Texas and available from the Internet by anonymous FTP from maxrad6.uthscsa.edu) to account for the proportion of blocks (fractions coarser than −6 phi). Due to the significant variations in clast shapes and geometries (for example, tabular or elongated clasts) observed in a single sample, the longest visible axes were used for size measurements of the blocks in vertical side-view on scaled photographs, as described by Karatson *et al.* (2002). Using a mean clast density, the volume percentages calculated were converted to mass percentages for combination with sieve analyses. The final mass percentages of each sample were plotted using the software GRADISTAT© (Blott & Pye, 2001) to calculate grain-size parameters. As it is difficult to apply Inman (1952) and Folk & Ward (1957) grain-size parameters (particularly the sorting $\sigma_{\emptyset}$, coefficient) to samples with a non-Gaussian and polymodal size distribution, parameters were calculated for individual categories, as described below (Table 2).

Table 2. Grain-size parameters and matrix component data of the studied samples.

		Grain size (wt%)					Matrix component (wt%)			Matrix component parameters					
Section	Unit	Blocks	Lapilli	Ash	Md_{ϕ}	σ_{ϕ}	Juvenile	Accidental lithics	Crystals + dense glass	Md_{ϕ} *juv.*	Md_{ϕ} *lith.*	Md_{ϕ} *cryst. + dg*	σ_{ϕ} *juv.*	σ_{ϕ} *lith.*	σ_{ϕ} *cryst + dg*
CS1	L6	34·5	24·1	41·4	−5·08	3·98	54·5	5·8	39·7	−0·23	0·22	1·42	1·19	1·47	1·43
	S1A	–	–	100·0	2·82	1·68	19·6	7·1	73·3	1·07	3·10	3·16	1·72	1·68	1·45
	L1A	26·1	23·7	50·2	−1·97	4·01	51·0	7·4	41·6	−0·25	0·12	1·36	1·21	1·49	1·51
CS2	L6	27·9	26·7	45·4	−3·44	3·95	54·4	8·0	37·6	−0·04	0·93	1·42	1·25	1·49	1·42
	S1A	–	0·7	99·3	3·90	1·07	8·2	9·7	82·1	2·65	3·95	3·98	1·99	0·94	0·85
	L1A	5·7	33·5	60·8	−0·78	3·46	47·9	15·9	36·2	−0·20	0·56	1·55	1·24	1·60	1·43
CS3	L5	25·6	24·9	49·5	−2·17	4·08	50·5	16·0	33·5	−0·13	0·35	1·68	1·17	1·58	1·44
CS4	L4	15·7	28·8	55·5	−1·14	3·85	45·2	15·3	39·5	−0·22	0·30	1·47	1·25	1·52	1·38
	S3	–	1·4	98·6	3·78	1·13	9·6	11·0	79·4	2·74	3·70	3·91	1·59	1·11	0·88
	L3	31·6	30·6	37·8	−5·03	3·99	42·6	17·1	40·3	−0·02	0·57	1·77	1·21	1·61	1·45
CS5	L2	21·2	37·8	41·0	−4·27	3·76	48·3	10·9	40·8	−0·26	0·34	1·50	1·23	1·50	1·37
	S1A	–	1·0	99·0	3·05	1·75	21·1	7·2	71·7	1·13	2·48	3·36	1·96	1·89	1·33
	L1A	26·7	31·0	42·3	−4·38	3·82	48·5	13·5	38·0	−0·28	0·47	1·49	1·25	1·59	1·48
	S1M	–	1·2	98·8	1·79	2·01	31·5	17·7	50·8	0·16	1·47	2·97	1·57	1·95	1·63
	L1M	15·6	25·5	58·9	−0·8	3·84	45·9	18·3	35·8	−0·08	0·57	1·86	1·24	1·63	1·48
CS6	L1A	22·5	39·0	38·5	−4·92	3·87	42·9	18·3	38·8	−0·23	0·52	1·63	1·31	1·62	1·47
	L1M	39·0	23·6	37·4	−5·75	4·06	41·8	21·1	37·1	−0·16	0·43	1·66	1·29	1·62	1·65
CS7	L2	13·9	43·1	43·0	−3·53	3·59	44·1	20·9	35·0	−0·10	0·46	1·60	1·30	1·54	1·33
	S1A	–	5·1	94·9	1·20	2·05	41·2	15·5	43·3	0·29	1·25	2·68	1·41	1·89	1·63
	L1M	11·2	23·6	65·2	−0·35	3·72	39·9	18·5	41·6	−0·08	0·71	1·61	1·30	1·63	1·47
CS9	L1A	33·0	27·6	39·4	−4·59	3·98	45·5	14·5	40·0	−0·22	0·56	1·69	1·23	1·62	1·41
	L1M	42·6	17·4	40·0	−5·27	3·95	42·0	18·4	39·6	0·02	0·50	1·69	1·29	1·62	1·42
CS11	L1A Top	–	29·8	70·2	−0·19	2·89	43·4	19·8	36·8	0·04	0·54	1·72	1·32	1·59	1·48
	L1A Middle	28·2	29·8	42·0	−3·54	3·75	47·6	18·4	34·0	−0·18	0·50	1·77	1·33	1·64	1·45
	L1A Base	6·2	28·9	64·9	−0·27	3·50	41·2	21·5	37·3	0·17	0·63	1·91	1·34	1·58	1·44
CS12	L1A	34·2	16·8	49·0	−2·31	4·21	42·7	14·2	43·1	−0·31	0·32	1·82	1·12	1·60	1·50
CS13	L1A	53·9	21·8	41·3	−7·12	3·78	38·0	12·5	49·5	−0·21	0·63	1·54	1·30	1·59	1·50
CS14	L1A	23·4	27·4	49·2	−2·21	4·06	47·5	13·8	38·7	−0·28	0·39	1·82	1·23	1·60	1·37
CS16	L1A Top	3·8	28·8	67·4	−0·32	3·32	40·8	16·3	42·9	−0·14	0·56	1·74	1·32	1·64	1·48
	L1A body	42·8	23·1	34·1	−6·17	4·00	44·0	17·5	38·5	−0·21	0·41	1·69	1·36	1·61	1·52
CS17	L1A	19·7	31·5	48·8	−2·37	4·09	43·6	19·2	37·2	−0·27	0·41	2·00	1·11	1·57	1·47
KA1	OB2	39·7	26·4	33·9	−6·12	3·93	40·3	19·7	40·0	0·01	0·69	1·61	1·39	1·55	1·46
KA2	OB2	–	35·9	64·1	−0·57	3·24	49·6	18·6	31·8	−0·01	0·57	1·86	1·31	1·61	1·51
	OB1	3·2	41·2	55·6	−1·20	3·33	53·5	17·5	29·0	−0·19	0·35	1·90	1·30	1·57	1·43
	S1	–	8·4	91·6	0·59	2·00	44·4	17·8	37·8	−0·09	0·68	2·18	1·29	1·70	1·53
KA3	OB1	18·2	31·5	50·2	−1·96	3·79	42·1	18·3	39·6	−0·18	0·72	1·57	1·35	1·65	1·47
IN1	OB1	23·9	23·6	52·5	−1·60	4·26	44·9	15·7	39·4	−0·04	0·56	1·81	1·36	1·62	1·58

Table 2. (*Continued*)

Section	Unit	Grain size (wt%)					Matrix component (wt%)			Matrix component parameters					
		Blocks	Lapilli	Ash	Md_{ϕ}	σ_{ϕ}	Juvenile	Accidental lithics	Crystals + dense glass	Md_{ϕ} *juv.*	Md_{ϕ} *lith.*	Md_{ϕ} *cryst.* + *dg*	σ_{ϕ} *juv.*	σ_{ϕ} *lith.*	σ_{ϕ} *cryst* + *dg*
IN2	OB2	25·6	23·9	50·5	−1·89	4·05	–	–	–	–	–	–	–	–	–
IN3	OB2	13·6	29·2	57·2	−0·92	3·73	42·9	19·5	37·6	−0·21	0·59	1·72	1·32	1·61	1·52
	S1	–	10·4	89·6	0·41	2·00	45·1	22·9	32·0	−0·09	0·60	1·98	1·31	1·65	1·55
IN4	OB2 Top	12·3	27·3	60·4	−0·67	3·74	41·8	19·5	38·7	0·11	0·60	0·75	1·39	1·64	1·49
	OB2 Base	–	30·8	69·2	−0·24	3·10	41·7	21·7	33·6	−0·01	0·49	1·81	1·34	1·63	1·43
KG1	OB2	27·1	30·9	42·0	−4·15	4·05	38·8	16·2	45·0	−0·17	0·76	1·56	1·36	1·67	1·45
KG2	OB2	33·7	32·4	33·9	−5·91	4·01	42·4	16·1	41·5	−0·13	0·86	1·93	1·36	1·75	1·46
KG3	OB2	7·8	27·9	64·3	−0·54	3·59	39·7	20·7	39·6	−0·20	0·72	1·91	1·33	1·69	1·46

Md_{ϕ} *juv.*, Md_{ϕ} *lith.* and Md_{ϕ} *cryst* + *dg* indicate median diameter values of juvenile, accidental lithics and crystals + dense glass components.
σ_{ϕ} *juv.*, σ_{ϕ} *lith.* and σ_{ϕ} *cryst* + *dg* indicate sorting values of juvenile, accidental lithics and crystals + dense glass components.
Md_{ϕ}, median diameter; σ_{ϕ}, sorting.

Matrix componentry analysis

Matrix componentry analyses were performed using a binocular microscope and point counting particles between −1 phi (2 mm) and 5 phi (32 μm). Approximately 100 grains were hand-picked for each grain-size fraction, corresponding to *ca* 700 grains per sample. Following the six main lithological categories identified from the deposit surface particle assemblage analysis in 2006 (Charbonnier & Gertisser, 2008), each hand-picked grain was assigned to one of the following categories: (i) juvenile fragments (grouping fragments from light and dark grey scoriaceous clasts, light grey dense clasts and dense, prismatically jointed clasts); (ii) loose crystals and dense glass; and (iii) accidental lithic fragments (hydrothermally altered and oxidized clasts). The volume percentages of each category from each fraction were converted to mass percentages using the corresponding mass value of the fraction from the grain-size analysis. The total mass percentages from the three different categories were then recalculated to 100%. This approach allows direct comparison of both the grain-size distribution and relative abundance of the three categories of different samples. The mass percentages for each sample were plotted using 'GRADISTAT' to calculate matrix component parameters (Table 2).

Coarse clast componentry analysis

The composition of coarse clasts in vertical deposit sections was determined in the field at the same sites sampled for grain-size analysis, but only for the basal avalanche and overbank deposits. The same grain-size fractions [3 to 10 cm (−4·9 to −6·6 phi) and coarser than 10 cm (−6·6 phi)] as those previously used for the deposit surface particle assemblage analysis were selected. Following the method described by Schwarzkopf *et al.* (2005), *ca* 20 to 30 clasts were counted for the fraction coarser than 10 cm, if present, and 30 to 40 for the fraction from 3 to 10 cm (Table 3). Due to the dimensions of the sample boxes used for granulometrical analysis, metre-sized blocks (coarser than −10 phi) were not included in the analysis.

Volume calculations

Volumes of the different flow deposits were calculated using the ArcGIS™ software 'Surface Analysis' tool (ESRI, Redlands, CA, USA) and the methods described in Charbonnier (2009).

Table 3. Coarse-clast lithology/componentry of the studied samples.

			Coarse clast components (%)									
Section	Unit	Clast size	Type 1	Type 2	Type 3	Type 4	Type 5	Type 6	Juvenile (types 1 to 4)	Accidental lithics (types 5 to 6)	Scoria (types 1 to 2)	Dense clasts (types 3 to 6)
CS1	L6	From 3 to 10 cm	63·3	16·7	10·0	0·0	10·0	0·0	90·0	10·0	80·0	20·0
		Coarser than 10 cm	60·0	3·3	13·3	0·0	23·3	0·0	76·7	23·3	63·3	36·7
	L1A	From 3 to 10 cm	50·0	6·7	10·0	0·0	23·3	10·0	66·7	33·3	56·7	43·3
		Coarser than 10 cm	33·3	3·3	16·7	0·0	36·7	10·0	53·3	46·7	36·7	63·3
CS2	L6	From 3 to 10 cm	63·3	26·7	3·3	0·0	6·7	0·0	93·3	6·7	90·0	10·0
		Coarser than 10 cm	33·3	30·0	13·3	0·0	16·7	6·7	76·7	23·3	63·3	36·7
	L1A	From 3 to 10 cm	46·7	10·0	6·7	0·0	23·3	13·3	63·3	36·7	56·7	43·3
CS3	L5	From 3 to 10 cm	56·7	0·0	13·3	3·3	13·3	13·3	73·3	26·7	56·7	43·3
		Coarser than 10 cm	36·7	0·0	23·3	0·0	30·0	10·0	60·0	40·0	36·7	63·3
CS4	L4	From 3 to 10 cm	46·7	13·3	13·3	6·7	10·0	10·0	80·0	20·0	60·0	40·0
		Coarser than 10 cm	16·7	20·0	23·3	3·3	16·7	20·0	63·3	36·7	36·7	63·3
	L3	From 3 to 10 cm	26·7	20·0	13·3	23·3	6·7	10·0	83·3	16·7	46·7	53·3
		Coarser than 10 cm	10·0	6·7	20·0	6·7	40·0	16·7	43·3	56·7	16·7	83·3
CS5	L2	From 3 to 10 cm	63·3	6·7	3·3	0·0	16·7	10·0	73·3	26·7	70·0	30·0
		Coarser than 10 cm	43·3	0·0	33·3	0·0	20·0	3·3	76·7	23·3	43·3	56·7
	L1A	From 3 to 10 cm	43·3	0·0	36·7	3·3	10·0	6·7	83·3	16·7	43·3	56·7
		Coarser than 10 cm	25·0	0·0	65·0	0·0	5·0	5·0	90·0	10·0	25·0	75·0
	L1M	From 3 to 10 cm	27·5	10·0	7·5	0·0	42·5	12·5	45·0	55·0	37·5	62·5
		Coarser than 10 cm	20·0	3·3	13·3	0·0	50·0	13·3	36·7	63·3	23·3	76·7
CS6	L1A	From 3 to 10 cm	36·7	10·0	20·0	0·0	20·0	13·3	66·7	33·3	46·7	53·3
		Coarser than 10 cm	6·7	0·0	53·3	0·0	33·3	6·7	60·0	40·0	6·7	93·3
	L1M	From 3 to 10 cm	50·0	16·7	13·3	0·0	16·7	3·3	80·0	20·0	66·7	33·3
		Coarser than 10 cm	33·3	10·0	16·7	0·0	26·7	13·3	60·0	40·0	43·3	56·7
CS7	L2	From 3 to 10 cm	23·3	23·3	26·7	6·7	13·3	6·7	80·0	20·0	46·7	53·3
		Coarser than 10 cm	30·0	10·0	10·0	0·0	40·0	10·0	50·0	50·0	40·0	60·0
CS7	L1M	From 3 to 10 cm	30·0	26·7	10·0	3·3	30·0	0·0	70·0	30·0	56·7	43·3
		Coarser than 10 cm	5·0	10·0	10·0	0·0	45·0	30·0	25·0	75·0	15·0	85·0
CS9	L1A	From 3 to 10 cm	26·7	26·7	10·0	6·7	20·0	10·0	70·0	30·0	53·3	46·7
		Coarser than 10 cm	30·0	23·3	10·0	0·0	20·0	16·7	63·3	36·7	53·3	46·7
	L1M	From 3 to 10 cm	33·3	30·0	13·3	6·7	10·0	6·7	83·3	16·7	63·3	36·7
		Coarser than 10 cm	26·7	3·3	16·7	0·0	43·3	10·0	46·7	53·3	30·0	70·0
CS11	L1A top	From 3 to 10 cm	33·3	20·0	20·0	13·3	10·0	3·3	86·7	13·3	53·3	46·7
	L1A mid	From 3 to 10 cm	33·3	16·7	6·7	26·7	13·3	3·3	83·3	16·7	50·0	50·0
	L1A base	From 3 to 10 cm	30·0	6·7	23·3	10·0	10·0	20·0	70·0	30·0	36·7	63·3
CS12	L1A	From 3 to 10 cm	36·7	3·3	16·7	3·3	36·7	3·3	60·0	40·0	40·0	60·0
		Coarser than 10 cm	26·7	0·0	26·7	0·0	36·7	10·0	53·3	46·7	26·7	73·3

Table 3. (*Continued*)

Section	Unit	Clast size	Coarse clast components (%)									
			Type 1	Type 2	Type 3	Type 4	Type 5	Type 6	Juvenile (types 1 to 4)	Accidental lithics (types 5 to 6)	Scoria (types 1 to 2)	Dense clasts (types 3 to 6)
CS13	L1A	From 3 to 10 cm	46·7	10·0	13·3	6·7	13·3	10·0	76·7	23·3	56·7	43·3
		Coarser than 10 cm	26·7	6·7	10·0	3·3	46·7	6·7	46·7	53·3	33·3	66·7
CS14	L1A	From 3 to 10 cm	60·0	0·0	6·7	6·7	20·0	6·7	73·3	26·7	60·0	40·0
		Coarser than 10 cm	53·3	0·0	6·7	6·7	26·7	6·7	66·7	33·3	53·3	46·7
CS16	L1A top	From 3 to 10 cm	46·7	0·0	16·7	0·0	26·7	10·0	63·3	36·7	46·7	53·3
		Coarser than 10 cm	43·3	0·0	13·3	0·0	26·7	16·7	56·7	43·3	43·3	56·7
	L1A body	From 3 to 10 cm	63·3	0·0	6·7	6·7	23·3	0·0	76·7	23·3	63·3	36·7
		Coarser than 10 cm	43·3	0·0	6·7	10·0	33·3	6·7	60·0	40·0	43·3	56·7
CS17	L1A	From 3 to 10 cm	63·3	0·0	6·7	6·7	23·3	0·0	76·7	23·3	63·3	36·7
		Coarser than 10 cm	43·3	0·0	6·7	10·0	33·3	6·7	60·0	40·0	43·3	56·7
KA1	OB2	From 3 to 10 cm	33·3	6·7	33·3	10·0	10·0	6·7	83·3	16·7	40·0	60·0
		Coarser than 10 cm	40·0	10·0	30·0	5·0	5·0	10·0	85·0	15·0	50·0	50·0
KA2	OB2	From 3 to 10 cm	47·5	20·0	15·0	0·0	12·5	5·0	82·5	17·5	67·5	32·5
	OB1	From 3 to 10 cm	42·5	7·5	17·5	2·5	22·5	7·5	70·0	30·0	50·0	50·0
KA3	OB1	From 3 to 10 cm	46·7	6·7	20·0	13·3	6·7	6·7	86·7	13·3	53·3	46·7
		Coarser than 10 cm	46·7	3·3	3·3	6·7	26·7	13·3	60·0	40·0	50·0	50·0
IN1	OB1	From 3 to 10 cm	46·7	10·0	6·7	13·3	20·0	3·3	76·7	23·3	56·7	43·3
		Coarser than 10 cm	33·3	6·7	6·7	10·0	33·3	10·0	56·7	43·3	40·0	60·0
IN2	OB2	From 3 to 10 cm	56·7	0·0	10·0	6·7	20·0	6·7	73·3	26·7	56·7	43·3
		Coarser than 10 cm	60·0	0·0	6·7	0·0	23·3	10·0	66·7	33·3	60·0	40·0
IN3	OB2	From 3 to 10 cm	42·5	7·5	2·5	2·5	30·0	15·0	55·0	45·0	50·0	50·0
		Coarser than 10 cm	40·0	10·0	0·0	6·7	30·0	13·3	56·7	43·3	50·0	50·0
IN4	OB2 top	From 3 to 10 cm	43·3	3·3	10·0	6·7	16·7	20·0	63·3	36·7	46·7	53·3
	OB2 base	From 3 to 10 cm	40·0	16·7	13·3	6·7	13·3	10·0	76·7	23·3	56·7	43·3
KG1	OB2	From 3 to 10 cm	66·7	6·7	6·7	0·0	6·7	13·3	80·0	20·0	73·3	26·7
KG2	OB2	From 3 to 10 cm	53·3	3·3	26·7	0·0	10·0	6·7	83·3	16·7	56·7	43·3
		Coarser than 10 cm	43·3	3·3	16·7	3·3	23·3	10·0	66·7	33·3	46·7	53·3
KG3	OB2	From 3 to 10 cm	46·7	3·3	16·7	0·0	26·7	6·7	66·7	33·3	50·0	50·0

Components: type 1 = light grey scoria; type 2 = dark grey scoria; type 3 = light grey dense clasts; type 4 = prismatically jointed clasts; type 5 = hydrothermally altered clasts; type 6 = oxidized clasts.
Juvenile components (scoria and cognate lithics) = types 1 to 4; accidental lithics = types 5 and 6; scoria = types 1 and 2; dense clasts (cognate and accidental lithics) = types 3 to 6.

Each unit identified in the stratigraphic sections has been assigned to one of the lobes recognized previously from the deposit surface. This way, each lobe has been divided into different zones of constant thicknesses. Volumes obtained for each polygon of the same lobe were then added together to obtain the overall deposit volume. This method provides a more accurate estimate of the overall deposit volume of the long-runout flows, which swept broader sectors with varying slopes and confinement, than those performed from the deposit surface (cf. Charbonnier & Gertisser, 2008).

STRATIGRAPHY

In the following sections, each stratigraphic section of the valley-filling and overbank deposits of the June 2006 BAFs is presented, together with results from the sedimentological analyses of each unit. To facilitate lateral and vertical facies correlations between different sections, three regional areas for the valley-filling deposits [proximal (sections CS1 to CS5), medial (sections CS6 to CS11) and distal (sections CS12 to CS17)], and three main depositional zones for the overbank deposits [Kaliadem/K. Opak area (sections KA1 to KA3), interfluve area (sections IN1 to IN4) and K. Gendol 2 (sections KG1 to KG3)] were distinguished.

Valley-filling deposits

Proximal area

Deposits in the proximal area between 1·5 and 3·5 km from the summit were only partly eroded during the first two rainy seasons following the eruption. Five stratigraphic sections (CS1 to CS5 in Fig. 2) were described along two main erosional channels and 10 depositional units were recognized. Sections and results from the sedimentological analyses of each unit are presented in Fig. 2 and Tables 2 and 3.

The two most proximal sections CS1 and CS2 are located at the beginning of the Gendol valley along the eastern wall, 2·3 and 2·8 km from the summit. These sections cut the deposits mostly parallel to the flow direction (Fig. 2) and exhibit the same deposit sequence with two massive, poorly sorted BAF units (L6 and L1A) with an interbedded finer grained unit (S1A). The topmost unit L6 is a dark-grey massive deposit, 2·5 (section CS1) to 4 m (section CS2) thick, made of angular to rounded blocks set in a layered lapilli–ash matrix. This poorly sorted, coarse-grained unit shows a weak, overall coarse-tail normal grading with a slight decrease in block content and size towards the surface of the deposits. Clast imbrication is well-developed with long axes of tabular and elongated clasts either oriented parallel to the flow direction {[a(p),b(i)]} or inclined upstream at angles of 10 to 30°. Layering of the matrix allows L6 to be divided into three sub-units separated by two fine-ash layers, each sub-unit showing apparent coarse-tail reverse grading (association of lithofacies mBLAms with mLA; Table 1). The unit pinches out *ca* 150 m downstream of section CS2. The basal unit L1A is a light-greyish to brownish, massive deposit >3·5 m thick (the base is not exposed) consisting of angular to sub-angular blocks in a fine lapilli–ash matrix. The unit is very poorly sorted and finer grained than unit L6. Two trains of blocks parallel to the bedding are present inside this unit at section CS1 (Fig. 2). Clast imbrication is common and long axes of elongated clasts are either flow-parallel {[a(p),b(i)]} or inclined in both directions at angles <30° (lithofacies mBLAss; Table 1). A thin (*ca* 1 cm), massive light-grey ash layer is found along the entire erosion channel downstream and separates the two previously described units (S1A unit, Fig. 2). This unit is well-sorted and shows a unimodal grain-size distribution with an abundance of medium-grained ash (lithofacies mA; Table 1). Loose crystals and dense glass are the most abundant matrix components of the S1A unit with an overall content reaching >73 wt% in the analysed sample (Table 2).

Sections CS3 and CS4 are located close to the channel centre, *ca* 3·1 and 3·4 km from the summit, respectively, inside less than 3 m deep, superficial erosion channels formed during the 2007 rainy season (Fig. 2). Unit L5 at section CS3 is a light-grey massive deposit of 2·5 m thickness made of angular to rounded blocks set in a lapilli–ash matrix. This poorly sorted, coarse-grained unit (lithofacies mBLAws; Table 1) shows a bimodal grain-size distribution with an abundance of medium-grained ash in the matrix (*ca* 50 wt% of the total deposit). Juvenile fragments are the most abundant component in the matrix and the grain-size distribution of the single matrix components is smoother and shows more defined modal, $\sigma_{\emptyset}$ and $Md_{\emptyset}$ values. The content of accidental lithics is high in the matrix (*ca* 16 wt%). Unit L4 at section CS4 is *ca* 2·7 m thick and shows a well-developed coarse-tail inverse grading with an increase in block content and size

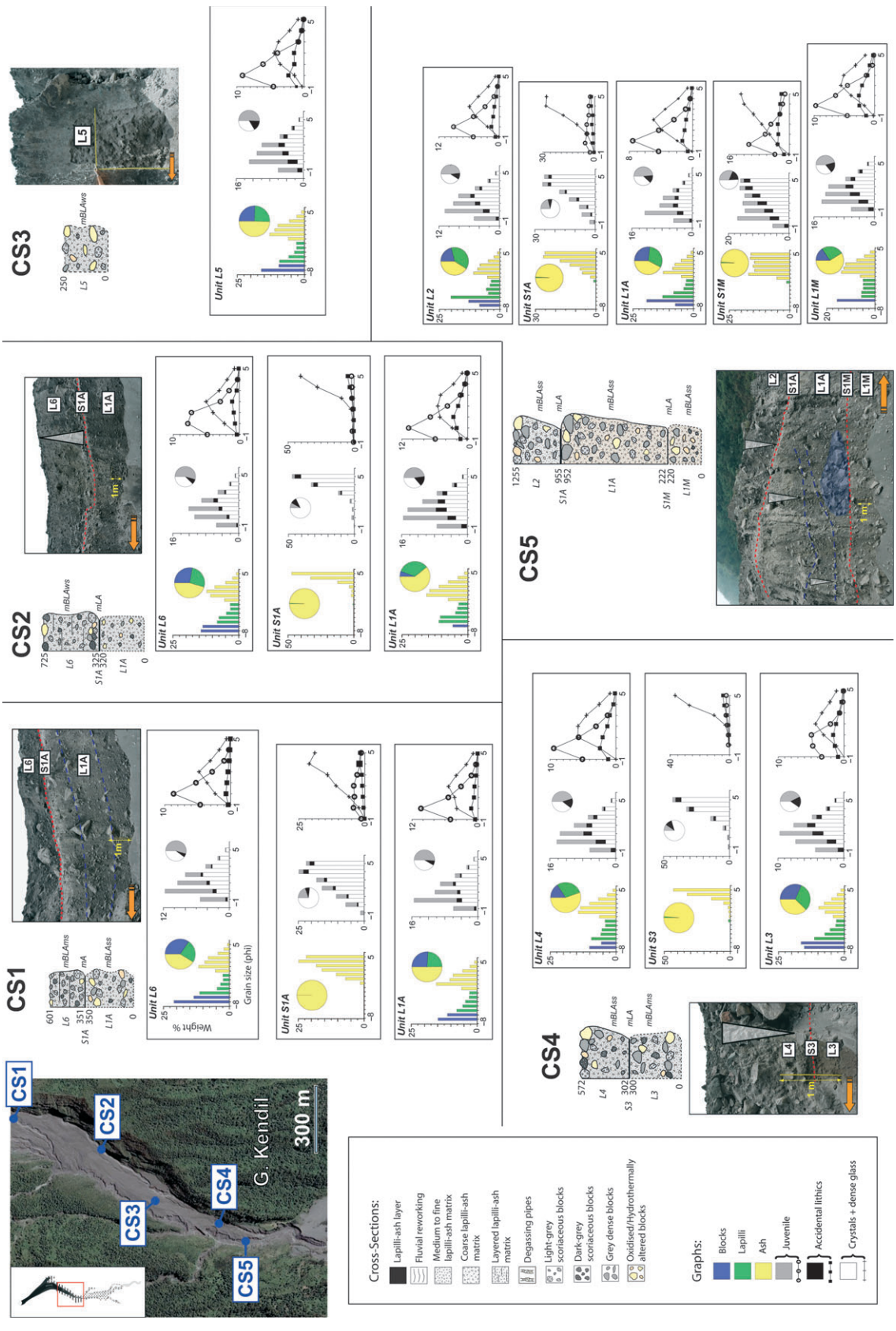

Fig. 2. Location of the five stratigraphic sections selected in the proximal area and results from their grain-size distributions with relative abundances of the different fractions (blue = blocks; green = lapilli; yellow = ash) and those of the three matrix components (grey/open circles = juvenile fragments; black/filled rectangles = accidental lithics; white/crosses = loose crystals + dense glass). Flow direction (orange arrow) and grading (white arrow) are also shown. The numbers in each section are in centimetres and the lithofacies codes of each depositional unit refer to Table 1.

towards the surface of the deposits (lithofacies mBLAss; Table 1 and Fig. 2). Matrix component analyses revealed a high proportion of juvenile fragments in the coarser fractions and a progressive increase in loose crystals and dense glass with decreasing grain size. The unit pinches out *ca* 100 m downstream of section CS4 just above a slope break at the surface of the deposits. The basal unit L3 is at least 3 m thick and is coarser than unit L4 with more than 30 wt% blocks in the analysed sample. A coarse-clast train is visible a few centimetres above the base of the section (Fig. 2), where flow-parallel clast imbrication {[a(p),b(i)]} occurs (lithofacies mBLAms; Table 1). A thin (*ca* 2 cm) light-grey to brownish lapilli–ash layer is present along the entire erosion channel and separates the two previous units at section CS4 (S3 unit, Fig. 2). Unit S3 is well-sorted and shows a unimodal grain-size distribution with an abundance of medium-grained to fine-grained ash (lithofacies mLA; Table 1). Loose crystals and dense glass are the most abundant components with an overall content reaching *ca* 80 wt%. The content of accidental lithics in the matrix is lower than in the matrix of the two previous units (*ca* 11 wt%, Table 2).

Section CS5, located *ca* 3·5 km from the summit in the middle of the valley (Fig. 2), represents one of the most complete exposures of the June 2006 deposits. Here, a *ca* 13 m deep erosion channel on the western side of the valley cuts through the deposits oblique to the flow direction for more than 300 m, exposing almost the entire sequence. The section is composed of three massive, poorly sorted BAF units with two finer grained units in between (Fig. 2). The major differences between the deposits of BAF units L2, L1A and L1M are their overall grain-size distributions and matrix composition (finer grained deposits with higher accidental lithic content in unit L1M), and the presence of two trains of blocks inside the *ca* 7 m thick unit L1A (lithofacies mBLAms for unit L2 and mBLAss for both units L1A and L1M; Table 1). A zone of coarse imbricated clasts is also visible at the base of unit L1A (Fig. 2). In areas without imbrication, the orientation of the long axes of tabular clasts follows the flow direction {[a(p),b(i)]}. The latter deposit fabric is present all along the exposure, irrespective of unit thickness variations. The brownish lapilli–ash layer S1A (lithofacies mLA; Table 1) is found along the entire erosion channel and serves as a stratigraphic marker to distinguish units L2 and L1A. Unit S1M is a thinner layer (<2 cm thick) that consists of a moderately sorted ($\sigma_{\emptyset}$ = 2·01), coarser grained ($Md_{\emptyset}$ = 1·79) deposit rich in medium-grained ash (lithofacies mLA; Table 1). The main differences compared with the previous units of the same facies are a polymodal grain-size distribution, a higher proportion of juvenile fragments (>30 wt%) and accidental lithics (>17 wt%), and a lower crystal and dense glass content (*ca* 50 wt%). This thin unit tends to thicken upstream towards the valley margin and is laterally replaced by a very faint ash layer, a few millimetres thick, towards the valley centre downstream.

Medial area

The constriction point in the Gendol valley, located 3·5 km from the summit, marks the boundary between the proximal and medial area (Fig. 1). The deposits in the medial area up to 5·0 km from the summit were eroded severely during the two rainy seasons following the eruption. Here, the valley is deep and narrow, and terraces on the eastern side of the channel constitute the only good exposures of the valley-filling deposits of the June 2006 BAFs. The lack of fresh exposure, combined with the great thickness of some units renders interpretations of the deposits difficult. Six stratigraphic sections (CS6 to CS11 in Fig. 3) were studied along two main erosional channels.

The three BAF units recognized in section CS5 (units L2, L1A and L1M) are also present in the medial area. Pronounced thickness variations occur within these three units, especially in areas where sudden changes of channel morphology and confinement occur. The topmost BAF unit L2 is only visible at section CS7, where its upper bounding surface is irregular and highly eroded (Fig. 3). The deposits show an overall coarse-tail normal grading (lithofacies mBLAws; Table 1). No blocks coarser than −7 phi have been found. The greyish matrix is rich in accidental lithics (*ca* 21 wt%, Table 2) but juvenile fragments are the most abundant component. Comparison with unit L2 at section CS5 shows enrichment in accidental lithics and dense clasts, and a decrease in the average particle size.

Unit L1A locally shows several stacked sub-units, separated by coarse-clast trains (association of lithofacies mBLAss; Table 1) and an absence of any erosive surfaces and/or deposition of fine ash between the sub-units (Table 1; sections CS6, CS9 and CS11; Fig. 3). In order to investigate vertical facies variations, unit L1A was sampled in three different areas of *ca* 2 m thickness from the base to the top (Fig. 3). Despite almost identical

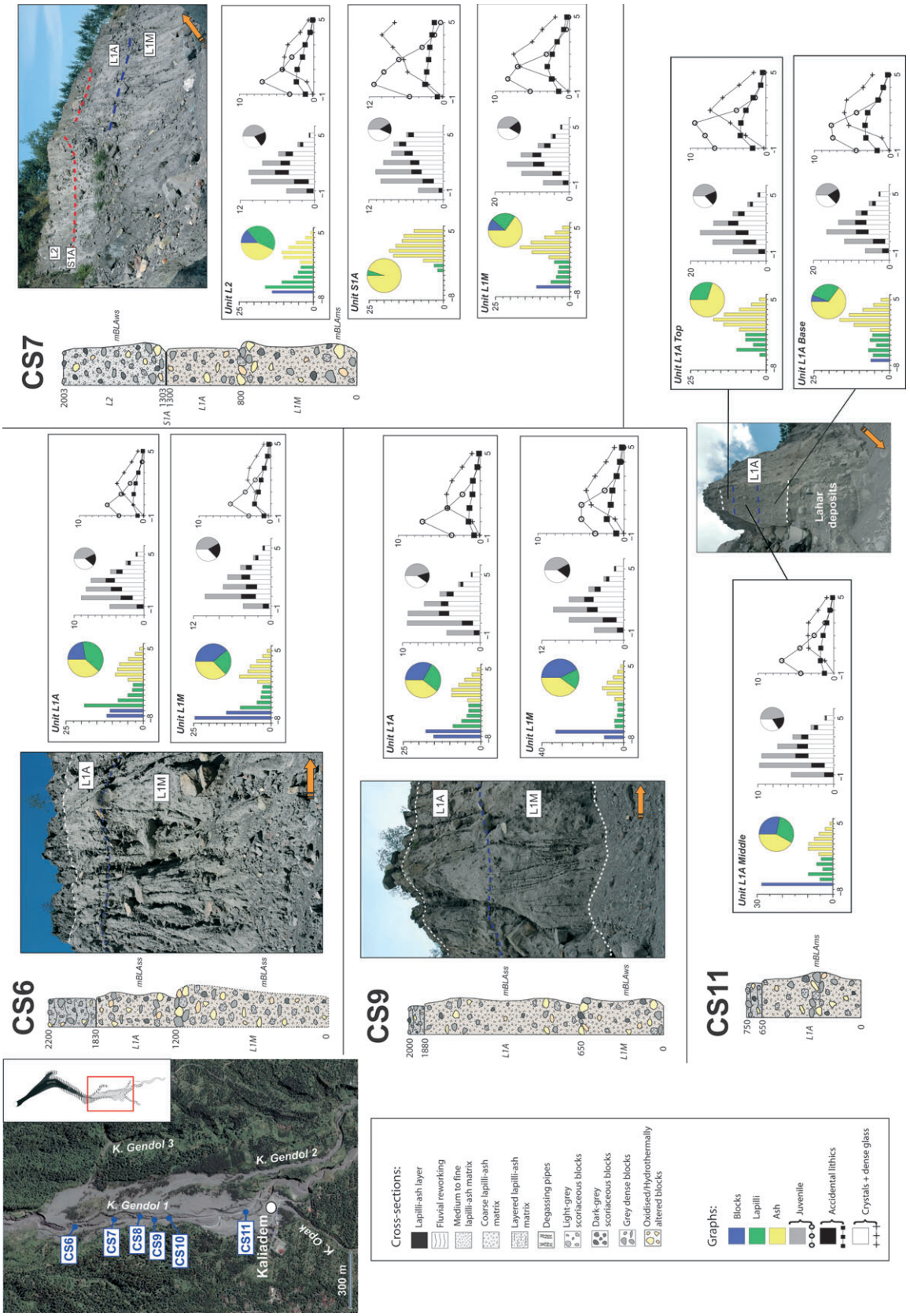

Fig. 3. Location of the six stratigraphic sections selected in the medial area and results from their grain-size distributions with relative abundances of the different fractions and those of the three matrix components. Same symbols as Fig. 2.

lithologies and clast contents (Tables 2 and 3), variations in the grain-size distribution are evident (Table 2). The middle part of the unit contains the highest proportion of coarse clasts that form a train where flow-parallel clast imbrications {[a(p),b(i)]} are common. The marginal deposit is finer grained and contains more brownish ash (>60% of the total sample weight) than the medial ones. The basal part is richer in dense clasts and accidental lithics than the other two. No blocks coarser than −7 phi occur in the entire unit. The upper erosional contact of unit L1A with the base of the reworked deposit at section CS6 is sharp and contrasts with the gradational basal contact with unit L1M observed in all sections, where individual boulders stick out at the bottom of the overlying bed (Fig. 3). The same deposit facies as that observed in unit S1M at section CS5 (lithofacies mLA; Table 1) is also found in the fine-grained and moderately sorted unit S1A on top of unit L1A at section CS7.

The basal unit L1M in the medial area differs from the overlying unit L1A as it has a lack of complex deposit architectures. L1M shows a downstream increase in maximum clast size alongside development of coarse-tail normal grading (transition from lithofacies mBLAms to mBLAws; Table 1), and a light-grey matrix with a higher content in accidental lithics (>18 wt%, Table 2). This unit has not been found downstream of section CS9, *ca* 4·3 km from the summit.

Distal area

Deposits in the distal area between 5·0 and 7·0 km from the summit were highly eroded during the two rainy seasons following the eruption. Based on field observations and analysis of high-resolution aerial photographs, fluvial reworking during the first rainy season removed more than 90% of the primary BAF deposits in a sector between Kaliadem (4·8 km from the summit) and the junction between K. Gendol 1 and K. Gendol 2 (6·0 km from the summit; Fig. 1). Sampling in the area >6·0 km from the summit was facilitated by the permanent daytime presence of Indonesian workers inside the valley, who extracted the recent volcanic products for building of infrastructures and roads; this resulted in the formation of a channel network that cut the 2006 deposits longitudinally and laterally (Fig. 4), and allowed the study of the internal deposit architecture in three dimensions.

Just below the junction between K. Gendol 1 and 2, a transverse gully cut the valley-filling deposits across their entire width (Fig. 4). The primary deposits have been replaced partially on top by lahar deposits, but good, *ca* 2 to 4 m high vertical exposures were still preserved at the base along the channel. Three sections extending from the western to the eastern side of the valley were selected (CS13, CS14 and CS15) to study lateral facies variations within unit L1A *ca* 6 km from the source (Fig. 4). There is an absence of stacked sub-units with coarse-clast trains, as observed in the proximal and medial areas, and significant variations in grain-size distribution and composition of the deposits over a lateral distance of only *ca* 120 m inside the channel. The major trend observed is coarse-clast enrichment in the deposits towards the channel centre (lithofacies mBLAms; Table 1). The mid-channel deposits contain more than 50 wt% blocks and are fines-depleted compared with the marginal deposits (Table 2).

Section CS16 is located *ca* 200 m before the end of the June 2006 deposits, *ca* 6·7 km from the summit. One of the best exposures occurred along a *ca* 200 m long transverse channel (Fig. 4), where *ca* 15 m of the primary deposits were exposed. Only one massive, *ca* 14 m thick BAF unit (L1A), surrounded by *ca* 1 m of reworked material, has been recognized along the channel. Sampling in the middle and at the top of unit L1A at section CS16 revealed distinct vertical facies variations (Fig. 4). Compared with all previous sections through unit L1A further upstream, the deposits left by the flow at section CS16 are much thicker and almost completely exposed. As in the previous sections, coarse-clast enrichment towards the middle part of the unit and the channel centre (lithofacies mBLAms; Table 1), a finer grained upper part with a reddish colouration of the matrix and abundant degassing pipes towards the deposit surface are present. The degassing pipes contain high proportions of oxidized and hydrothermally altered, lapilli-sized clasts and are depleted in ash-sized fragments; they are typically <2 m long and 50 cm wide and tend to widen towards the surface (Fig. 4). The superficial structures of these pipes were found on the deposit surface during the 2006 survey (Charbonnier & Gertisser, 2008), confirming their pristine nature.

The most distal channel section is *ca* 50 m from the end of the 2006 deposits, at the outside of a pronounced bend in K. Gendol 1 (Fig. 4). The deposit is thinner and richer in ash compared with that at section CS16, *ca* 200 m upstream. No clasts coarser than −8 phi have been found and the finer grained, upper part of the unit is missing.

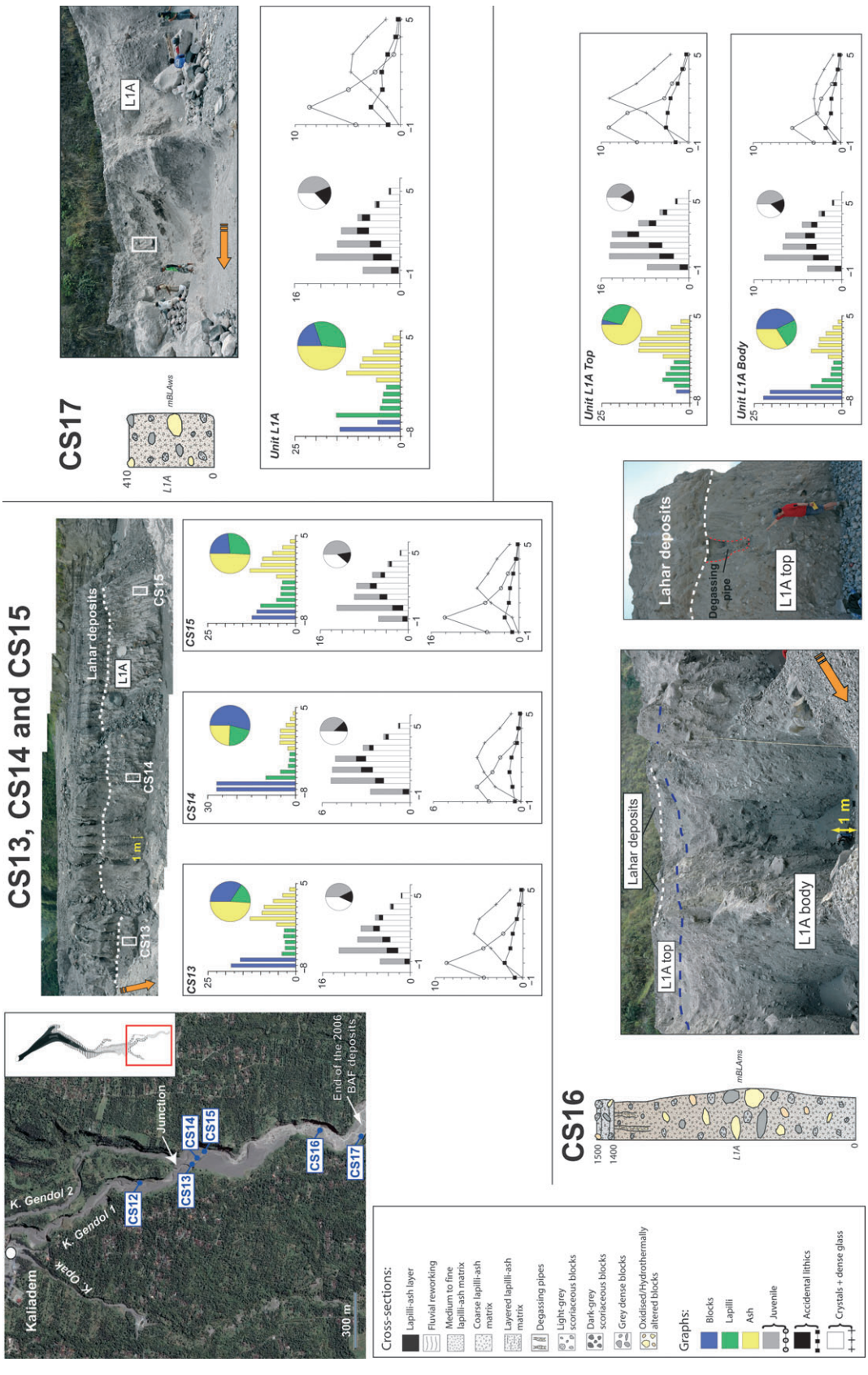

Fig. 4. Location of the six stratigraphic sections selected in the distal area and results from their grain-size distributions with relative abundances of the different fractions and those of the three matrix components. Same symbols as Fig. 2.

Overbank deposits

Interfluve area

Four stratigraphic sections were selected on the interfluve area (between K. Gendol 1 and 2) of the overbank deposits of the June 2006 BAFs. These sections are labelled, from proximal to distal reaches, sections IN1 to IN4 (Fig. 5).

Section IN1 represents the most proximal exposure of the overbank deposits. It is located *ca* 3·6 km from the summit on the interfluve area, just below the first overspill site that coincides with the presence of a *ca* 30 m high terrace that faces the flow direction. Erosion during the first rainy season cut a channel into the interfluve deposits parallel to the flow direction where the *ca* 3 m thick unit OB1 is exposed (Fig. 5). The proximal overbank deposits are characterized by strong coarse-tail reverse grading and preferred clast orientation (lithofacies mBLAss; Table 1). The development of a lower, coarse-clast-free part, >50 cm thick, could explain the high ash content found in the analysed sample (*ca* 52 wt%). The matrix of unit OB1 contains abundant juvenile fragments and loose crystals and dense glass (Table 2).

Sections IN2 and IN3 are located at the western margin of the central interfluve area, *ca* 4·5 km from the summit (Fig. 5). Section IN3 shows a complete exposure of the overbank deposits, whereas section IN2 only cuts through their upper part. The sections represent a combined vertical exposure of *ca* 6 m with two massive, poorly sorted units (OB1 and OB2) overlying a thin, finer grained unit at the base (Fig. 5). The contacts between the three units are gradational and no erosive surfaces and/or deposition of fine ash between the units have been found. The uppermost unit OB2 (*ca* 1·5 m thick) shows similar deposit facies in the two sections with very poorly sorted ($\sigma_{\emptyset}$ = 4·052), coarse-grained deposits ($Md_{\emptyset}$ = −1·894 with *ca* 25 wt% blocks) that exhibit coarse-tail reverse grading (lithofacies mBLAss; Table 1 and Fig. 5). The ash content represents *ca* 50 wt% of the total deposit mass and the matrix is essentially composed of medium-grained ash. No matrix component analyses have been performed, but coarse-clast componentry indicates a high proportion of juvenile and scoriaceous clasts in the grain-size fractions coarser than 10 cm (Table 3). The middle unit OB1 (*ca* 2·5 m thick) consists of a finer grained deposit than unit OB2 (Table 2). No blocks coarser than −7 phi have been found and the ash content represents >57% of the total deposit weight. The content of accidental lithics is relatively high in the matrix (19·5 wt%). The deposits show an enrichment of fines towards the contact with the fine-grained unit S1 (Fig. 5). The basal unit S1 is a massive, moderately sorted ($\sigma_{\emptyset}$ = 1·998) and fine-grained ($Md_{\emptyset}$ = 0·41 with *ca* 90 wt% ash) lapilli–ash layer of *ca* 15 cm thickness that exhibits a unimodal grain-size distribution (lithofacies mLA; Table 1 and Fig. 5). A low abundance of crystals and dense glass contrasts with the high accidental lithic content (*ca* 23 wt%) of the matrix. Unit S1 mantles the irregular underlying topographic surface where strong thickness variations occur a few metres downstream. No stratification and/or cross-bedding has been observed.

Section IN4 is located *ca* 4·8 km from the summit at the distal, western side of the central interfluve area (Fig. 5), opposite the channel section CS11. Here, a *ca* 100 m long erosion channel cut the upper part of the overbank deposits. A vertical exposure of *ca* 2 m shows one massive, poorly sorted unit (OB2). Two samples were collected from the upper and lower parts of the unit. Sampling of the entire uppermost unit OB2 revealed vertical facies variations, including an increase in the abundance and size of dense blocks, a decrease in sorting and ash content and a higher proportion of crystals and dense glass, and a lower accidental lithic content in the matrix from base to top (lithofacies mBLAss; Table 1). Longitudinal facies variations of unit OB2 consist of better sorting, enrichment in fines and depletion in blocks downstream.

Kaliadem/Kali Opak area

Located on the western interfluve area of K. Gendol 1, Kaliadem village has been buried by overbank deposits emplaced in three distinct geomorphological environments: (i) two proximal 'wedge-shaped' overbank deposits at the edge of the valley margins where the basal avalanche of the 14 June BAFs was able to leave the channel; (ii) an interfluve overbank deposit that was emplaced further away from the valley margins in an unconfined area; and (iii) a re-channelled overbank deposit where the associated flow was subsequently channelled into the adjacent Opak valley to the south-west of the village. Three stratigraphic sections were studied in this area (KA1 to KA3 in Fig. 5).

The most proximal section KA1 is located *ca* 4·4 km from the summit and corresponds to the third overspill site where the 14 June p.m. flow was able to run over the channel confines of

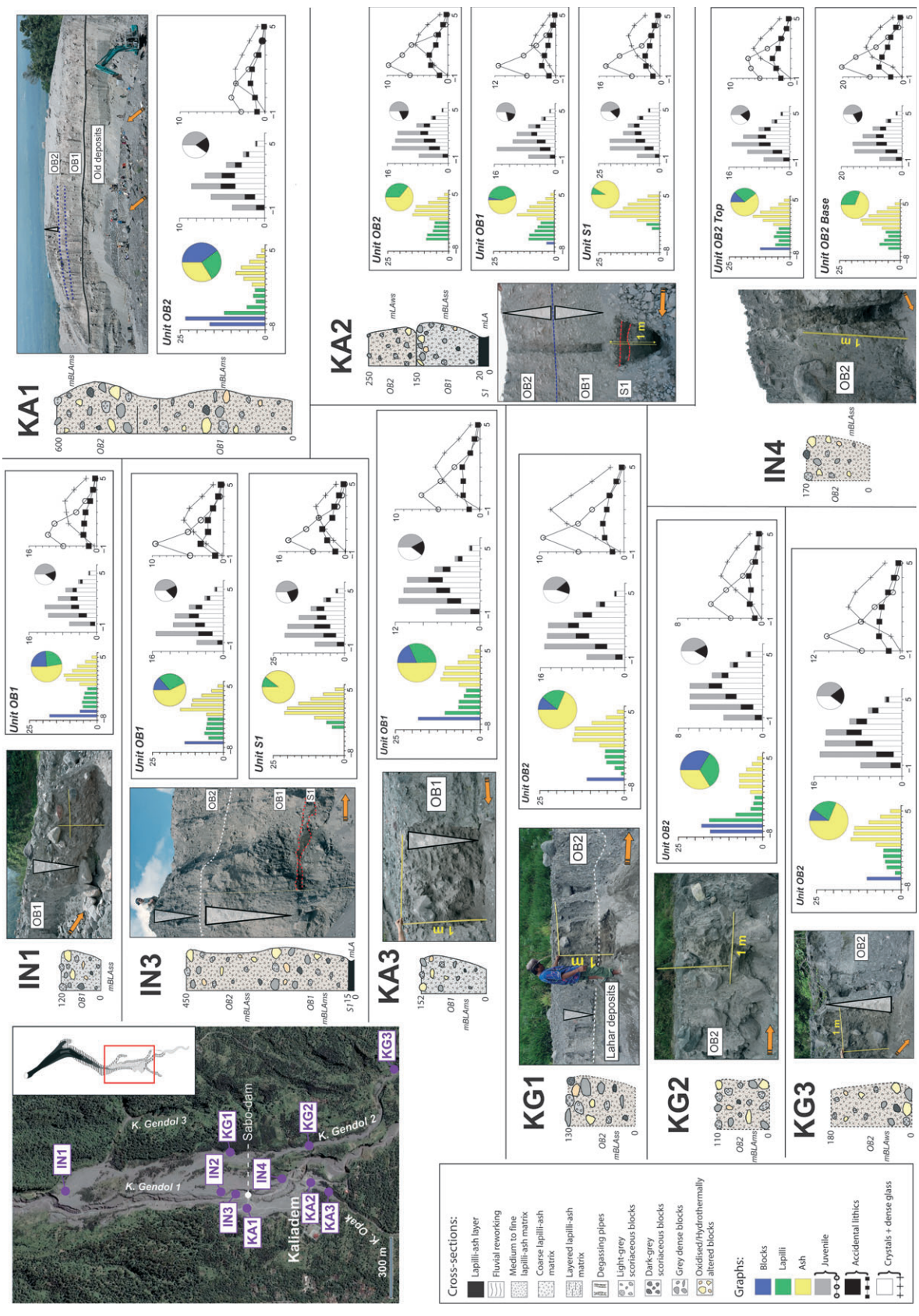

Fig. 5. Location of the ten stratigraphic sections selected in the overbank deposits of the June 2006 block-and-ash flows and results from their grain-size distributions with relative abundances of the different fractions and those of the three matrix components. Same symbols as Fig. 2.

K. Gendol 1 (Fig. 1). Intense erosion during the first post-eruption rainy season exposed a complete deposit sequence immediately upstream of the sabo-dam at the western edge of the valley margin (Fig. 5). Here, a *ca* 15 m high cliff shows the proximal 'wedge-shaped' 2006 overbank deposits at the top, overlying a soil layer with older deposits in the lower half of the section (Fig. 5). The soil layer corresponds to the ground level of the interfluve area before the 14 June events. The 2006 overbank deposits are *ca* 6 m thick and composed of two stacked units (OB1 and OB2) separated by a *ca* 1 m thick, fine-grained layer depleted in coarse clasts (association of lithofacies mBLAms; Table 1). A detailed log along the cliff has been carried out, but only the topmost unit OB2 has been sampled. Some of the facies variations observed between unit OB1 and OB2 at section IN3 have also been noticed at section KA1 (for example, the finer grained nature of the unit OB1). Lateral facies variations of unit OB2 between the two sections include a greater abundance of dense blocks, a higher proportion of accidental lithics in the matrix and a change from reverse to normal coarse-tail grading (transition from lithofacies mBLAss to mBLAms; Table 1).

Section KA2 is located inside Kaliadem village *ca* 4·8 km from the summit (Fig. 5), *ca* 100 m downstream from the fourth overspill site where the 14 June p.m. flow caused the heaviest damage to the houses (Fig. 1). Here, erosion exposed the 2006 deposits along a *ca* 50 m long and *ca* 3 m deep section. Two stacked units (OB1 and OB2) were identified, separated by a fine-grained interface and overlying a *ca* 20 cm thick lapilli–ash layer (unit S1) at the base (association of lithofacies mLAws with mBLAss and mLA; Table 1). This deposit sequence overlies old BAF deposits with a soil layer at the base. No soil has been found between the 2006 overbank deposit and the old BAF unit. This section exposed the same two stacked units OB1 and OB2 as those recognized at section KA1. Deposit facies variations between these two sections include a decrease in thickness and coarse clasts inside both units and the development of coarse-tail reverse grading in unit OB1. The matrix of unit OB2 shows a reddish colouration due to thermal oxidation. The basal unit S1 is a *ca* 20 cm thick, moderately sorted, lapilli–ash layer that shows a unimodal grain-size distribution (lithofacies mLA; Table 1 and Fig. 5). The deposit is rich in medium-grained ash. Accidental lithic content in the matrix is similar to that in unit OB1, but crystals and dense glass are more abundant (Table 2). The base of unit S1 mantles the pre-topographic surface and the contact with the underlying old BAF deposits is erosional.

Section KA3 is located inside the Opak river valley, *ca* 5·0 km from the summit and *ca* 200 m downstream of section KA2 (Fig. 5). Here, an overbank pyroclastic flow produced during the overspill of the 14 June p.m. flow at sites 3 and 4 (Fig. 1) subsequently was channelled into the valley to the south-west of the village and travelled for another 800 m downstream. Intense erosion in 2007 replaced the primary overbank deposits in the medial and distal parts of the Opak River with lahar deposits. The best exposures are situated along a proximal erosion channel that cut though the overbank deposits parallel to the flow direction. The overbank deposits in K. Opak show only one massive, poorly sorted and reversely graded unit (lithofacies mBLAss; Table 1). The facies transition of unit OB1 from the interfluve to the Opak valley (sections KA2 and KA3) is associated with an increase in block content and a slightly higher accidental lithic content in the matrix and the coarse fractions analysed.

Kali Gendol 2

Three stratigraphic sections of the overbank deposits were selected in the proximal, medial and distal areas of K. Gendol 2 (KG1 to KG3, Fig. 5). The most proximal section is located on the eastern side of the valley, *ca* 4·4 km from the summit. Here, the channel is broad and shallow and only the marginal primary deposits have been preserved after the first rainy season following the eruption. A complete exposure was available in a deep erosion channel a few tens of metres downstream and showed the basal contact between the 2006 deposits and an underlying soil layer (Fig. 5). The vertical exposure is *ca* 1·3 m high and shows only one massive unit (OB2) that consists of sub-angular to rounded blocks in a brownish, medium-ash matrix (Fig. 5). Other deposit features include strong coarse-tail reverse grading with a lower coarse-clast free zone and tabular clasts oriented either parallel to the base or sub-parallel to the channel wall (lithofacies mBLAss; Table 1). Section KG2 is located *ca* 400 m downstream of section KG1, in the centre of K. Gendol 2 (Fig. 5). Here, the valley is narrow and sinuous and an erosion channel cut the upper part of the overbank deposits parallel to the flow direction. The basal part of the deposits has been buried by lahar deposits that partially filled the channel. The most distal section is

located *ca* 5·6 km from the summit, on the eastern side of the valley (Fig. 5). Immediately upstream of section KG3, two sharp bends at *ca* 90° are present in the valley and the section is situated at the outside of the second bend. Transition from lithofacies mBLAss to mBLAms and mBLAws (Table 1) occurs between the overbank deposits exposed from sections KG1 to KG3. These include maximum clast size and deposition in the medial area, transition from reverse to normal coarse-tail grading from the proximal to the distal reaches, a decrease in crystal and dense glass content and an overall increase in the concentration of accidental lithics in the matrix downstream.

DISCUSSION

Longitudinal and lateral facies variations and correlations

Correlations between stratigraphic sections from the valley-filling and overbank deposits are presented in Fig. 6. Only a few correlations can be made between units from sections located in the proximal area of the valley-filling deposits. The most proximal lobate deposits (lobes 9, 8 and 7), with individual thicknesses <2·5 m (Charbonnier & Gertisser, 2008), are not exposed along the erosional channels. However, deposits of all the other lobes identified during the 2006 survey are represented in one or more sections (units L6 to L1A, Fig. 6). Even deposits from the 14 June a.m. flow (unit L1M), buried by later flows, had been exposed in the medial area after the first rainy season following the eruption. Comparisons with both monitoring data (BGVN, 2007) and surface observations (Charbonnier & Gertisser, 2008) support the interpretation that only deposits from the 14 June p.m. flow (unit L1A) are present at distances >4·5 km from the summit. In fact, only three BAF units, corresponding to the deposits from lobe 2 and the two flows of 14 June (L2, L1A and L1M), were recognized at a distance >3·5 km from the summit. Significant thickness variations have been observed within the valley-filling deposits of these units on a scale of a few tens of metres, especially in the medial area, where sudden changes in channel morphology and confinement occur. These three units show a similar downstream increase in thickness and maximum clast size before decreasing again in the lowermost (most distal) section. While the area of maximum deposition and clast size of units L2 and L1M occurs at *ca* 4 km from the source, thicknesses >14 m and individual boulders of *ca* 3 m diameter have been found within unit L1A around section CS16, *ca* 6·7 km from the summit. This indicates that varying modes of deposition are also determined by the flow conditions during transport (velocity and regime) and not only by the effects of local slope and confinement.

Comparison between the grain-size distributions of different units from different sections is almost impossible, as they often vary substantially downstream (for example, unit L1A). However, grain-size variations within units L4, L5 and L6, exposed in the proximal area, could be investigated, as no facies variations have been observed further downstream. These three units correspond to the deposition of three discrete BAFs with successively decreasing runout distances (Fig. 1). All these units are poorly sorted and show two sub-populations with a bimodal grain-size distribution (Fig. 7A). Successive deposition of the three flows led to an increase in median diameters ($Md_{\emptyset}$) from −1 to −5 phi and a decrease in the ash content from *ca* 55 to 41 wt%. These trends reflect the decreasing effects of particle break-up and collision during flow transport and emplacement towards the end of the eruption. The low content of accidental lithics, together with the abundance of scoriaceous juvenile clasts, indicates flow generation by short, single collapses of fresh material from the 2006 lava dome.

In the medial area, the sections around Kaliadem village depict local facies variations within both the valley-filling deposits (section CS11, Fig. 3) and the overbank deposits (section KA2, Fig. 5) derived from a single parent flow (i.e. L1A from 14 June p.m.). Cumulative frequency size distributions of each unit are shown in Fig. 7B. Proximal overbank deposits of unit OB2 at section KA1 (Fig. 5) are added for comparison. Units OB1, OB2 and S1 are associated with the deposition of two successive overbank flow pulses during the overspill of the 14 June p.m. flow on the western interfluves. Except for unit S1, which is moderately sorted with a unimodal distribution, all units show the same mBLAms lithofacies with two sub-populations and a polymodal distribution (Fig. 7B). The wide range of median diameters ($Md_{\emptyset}$ from −6·1 to 0·6 phi) and ash contents (from *ca* 34 to 92 wt%) within the deposits reflect the variability of deposits left from the passage of a single, sustained current over a small area during unsteady flow conditions. In addition, grain-size distributions from the overbank deposits show greater variations than

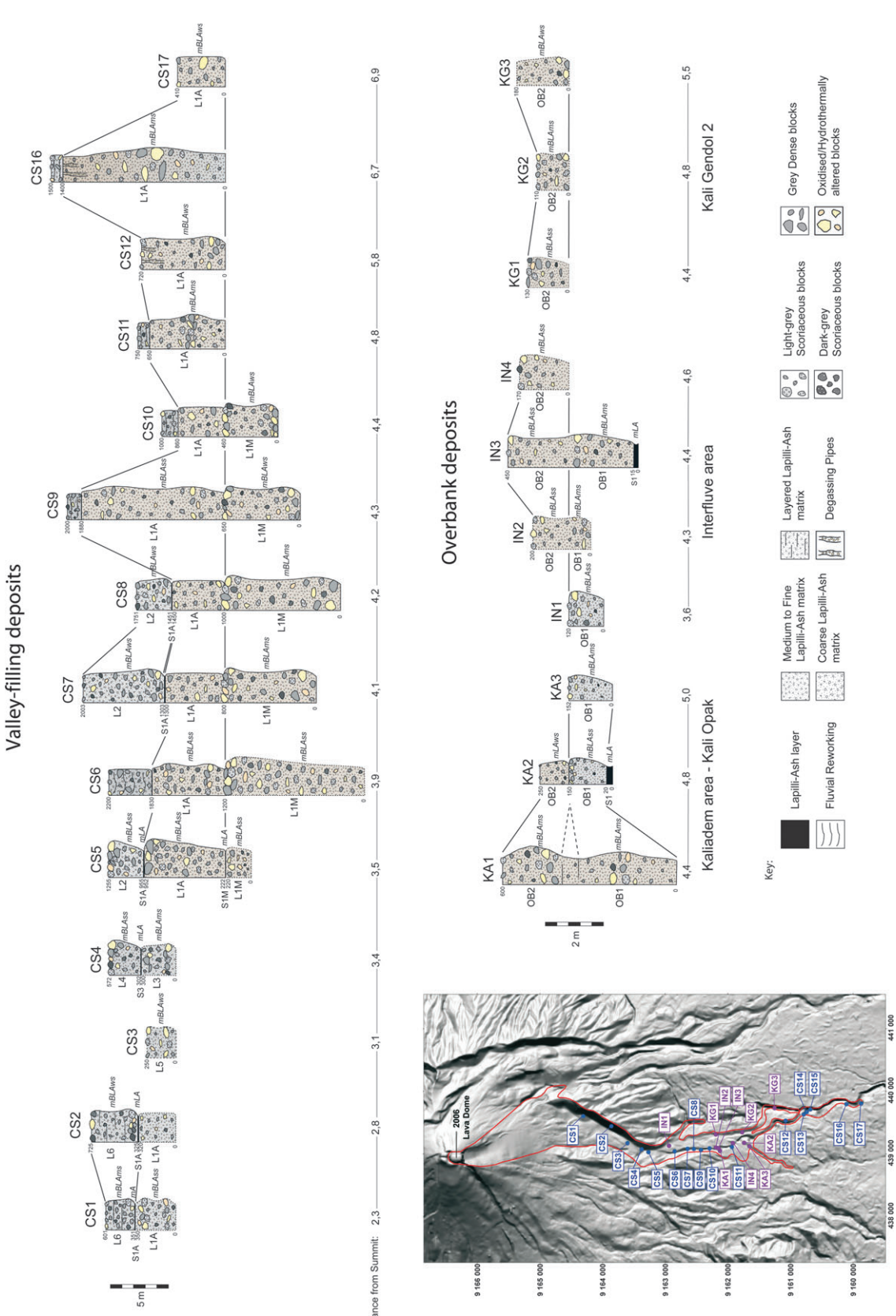

Fig. 6. Correlations between stratigraphic sections from the valley-filling and overbank deposits of the June 2006 block-and-ash flows. The inset map shows the locations of the different sections in the Gendol drainages. Channel sections CS13 to CS15 from the transverse gully in the distal area were omitted for clarity. The overbank sections were grouped by geographical location (Kaliadem area, interfluve and Kali Gendol 2). Lithofacies codes are also shown on the right-hand side of each depositional unit. See Table 1 for explanation.

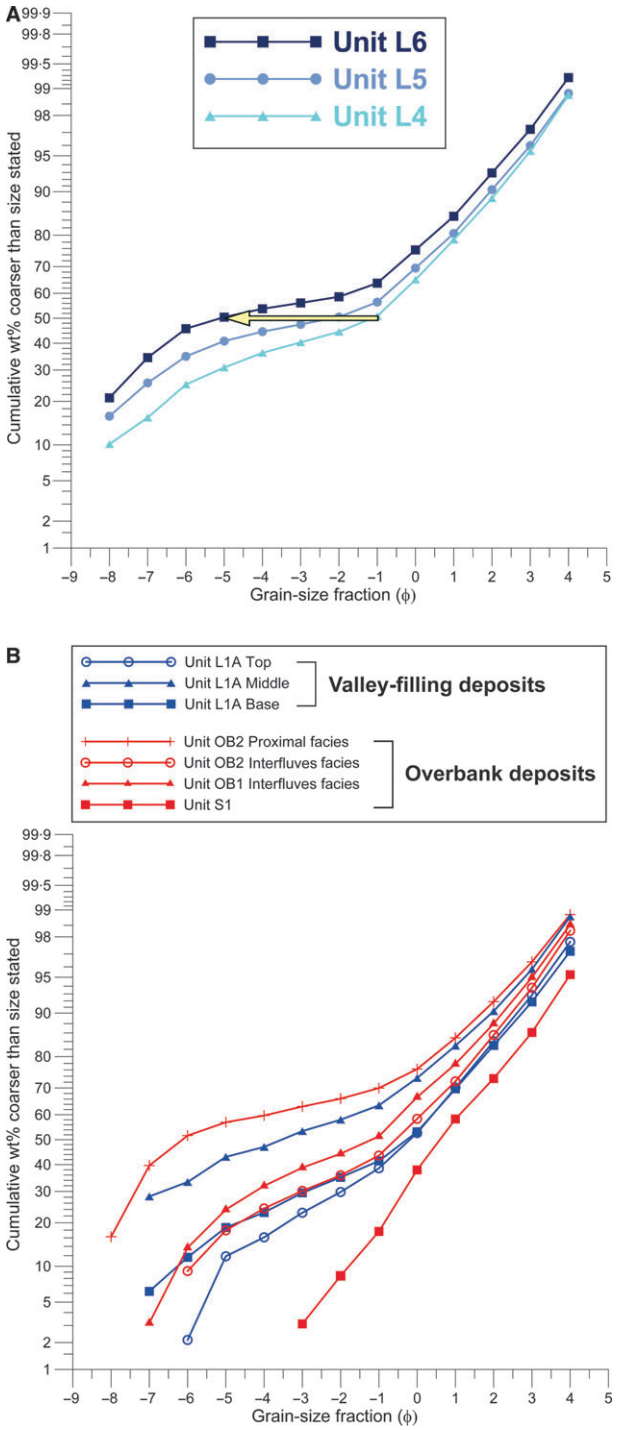

Fig. 7. (A) Cumulative frequency size distributions of lobe deposits in the proximal area (units L4 to L6), showing the increase in median diameters (yellow arrow). (B) Cumulative frequency size distributions showing grain-size variations between valley-filling and overbank deposits derived from the same parent flow (14 June p.m.) in the medial area (*ca* 4·8 km from the summit, Kaliadem village).

those from the valley-filling deposits (Fig. 7B). While the interfluve overbank deposits of units OB1 and OB2 are clearly derived from the basal avalanche deposits (similar frequency size distribution profiles on Fig. 7B), the proximal overbank deposits of unit OB2 and the fine-grained basal overbank layer S1 exhibit two extreme grain-size distributions. The great variability of frequency size distributions in the overbank deposits is related directly to clast segregation processes during individual BAF forming events. The coarse nature of the proximal overbank deposits on the outer bank of K. Gendol 1, combined with the presence of coarse-clast-depleted deposits in the upper part of the valley-filling section (Fig. 7B), may be due to processes of clast segregation that occurred inside the channelled flow when it impinged on the western valley margin. At this location, only the upper and marginal part of the basal avalanche enriched in coarse, low-density clasts would have been able to escape from the confines of the channel during the passage of each flow pulse at the key sites identified on Fig. 1. This observation implies a density stratification in the basal avalanche that has already been inferred for the 1994 and 1998 Merapi flows (Schwarzkopf *et al.*, 2005) and for similar flows elsewhere (e.g. Lube *et al.*, 2007). Massive deposition during rapidly waning flow conditions resulted in the extreme grain-size distributions observed in the associated overbank deposits at the edge of the valley margin. In this model, each pulse developed within the basal avalanche represents the highest stage-level of the flow that controls its ability to overspill the valley margins. The presence of the massive, fine-grained lapilli–ash layer S1 at the base of unit OB1 is interpreted as an ash-cloud deposit left from the passage of an ash-cloud surge from the 14 June p.m. BAF.

Sedimentological characteristics of the June 2006 deposits

In addition to the three main types of deposits recognized (valley-filling, overbank and ash-cloud surge), the samples were divided into different categories based on their lateral and longitudinal position in the Gendol valley, following the method described by Miyabuchi (1999) for the 1991 Unzen BAF deposits. The main valley-filling deposits are those located in the axial region of the channel and the marginal deposits are those of the peripheral areas.

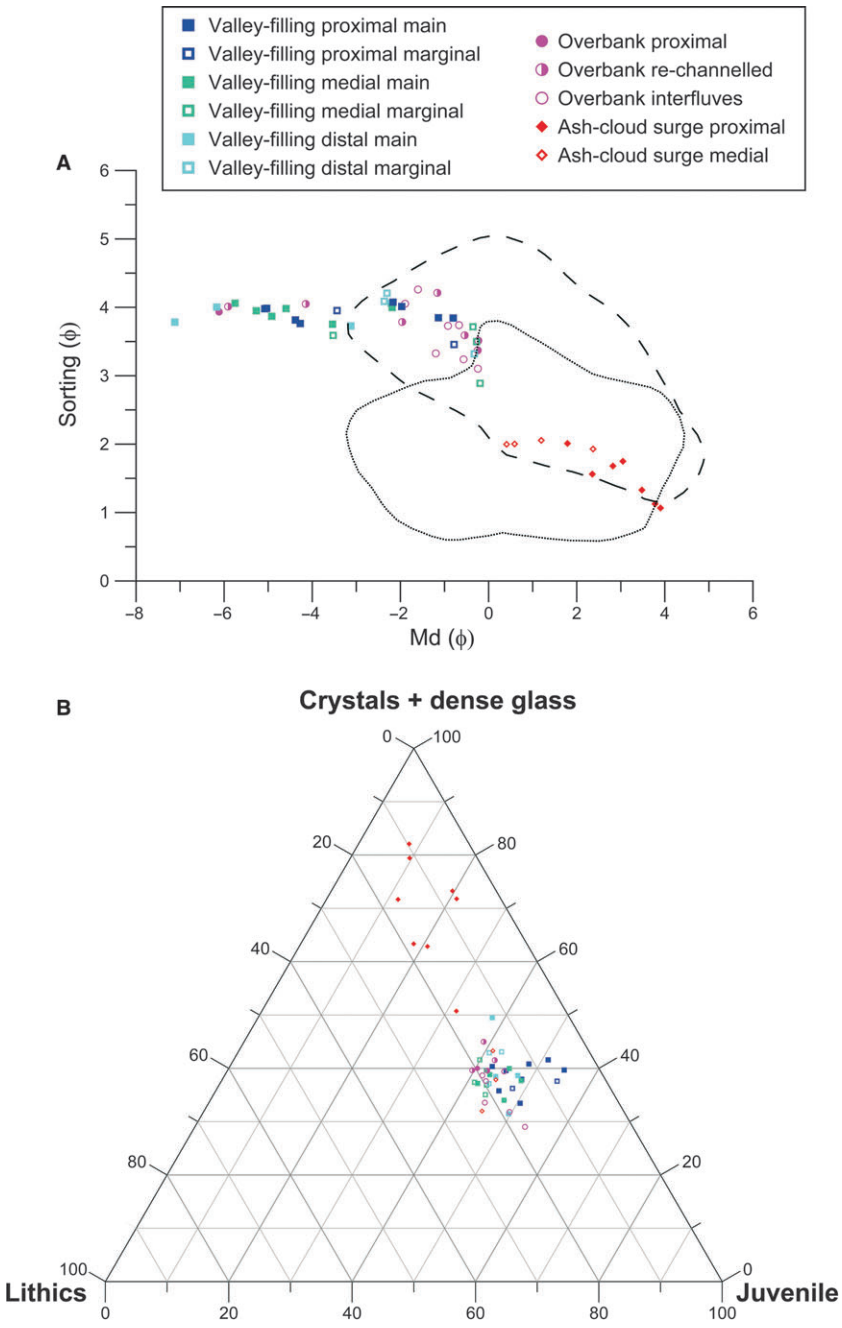

Fig. 8. (A) Plot of median diameter ($Md_{Ø}$) versus sorting coefficient ($\sigma_{Ø}$) for the different June 2006 BAF deposits. Samples from valley-filling deposits are classified given their lateral and longitudinal position in the Gendol valley, the main valley-filling deposits being those located in the axial region of the channel and the marginal deposits those of the peripheral areas. Overbank deposits are grouped into three distinct geomorphological environments: proximal 'wedge-shaped' overbank deposits at the edge of the valley margins, interfluve overbank deposits that were emplaced further away from the valley margins in an unconfined area, and a re-channelled overbank deposit where the associated flow subsequently was channelled into the adjacent valleys. Outline areas represent the 1% contour fields of Walker (1971, 1983) for pyroclastic flow (dashed line) and pyroclastic surge (dotted line) deposits. (B) Ternary diagram showing the relative abundances of the three matrix components (accidental lithics, juvenile fragments and loose crystals + dense glass) in the different samples from the June 2006 BAF deposits.

The same approach is used for the overbank and ash-cloud surge deposits (Fig. 8). Using this approach, the June 2006 BAF deposits are separated into 11 categories that are plotted on a diagram of median diameter ($Md_{Ø}$) versus sorting coefficient ($\sigma_{Ø}$), as described by Walker (1971) (Fig. 8A).

Figure 8A illustrates the coarser nature and poorer sorting of the valley-filling deposits ($Md_{Ø}$ from −7·1 to −0·3 phi, average = −3·1 phi; $\sigma_{Ø}$ average = 3·8) and the overbank deposits ($Md_{Ø}$ from −6·1 to −0·2 phi, average = −1·8 phi; $\sigma_{Ø}$ average = 3·7) relative to the ash-cloud surge deposits ($Md_{Ø}$ from 0·4 to 3·9 phi, average = 2·3 phi; $\sigma_{Ø}$ average = 1·7). Samples from the valley-filling and overbank deposits mostly plot within the pyroclastic flow field of Walker (1971), although some of them are much coarser grained (Fig. 8A); this is due to the fact that the full grain-size distributions of each sample (from −8 to 5 phi) have been taken into account during calculation of the grain-size parameters, producing coarser distributions than those reported by Walker (1971). With a few exceptions, the

marginal valley-filling deposits are finer grained and better sorted (Md_{ϕ} average = −1·5 phi; σ_{ϕ} average = 3·6) than the deposits from the axial regions (Md_{ϕ} average = −3·9 phi; σ_{ϕ} average = 3·9). The main valley-filling deposits show a minor downflow increase in average median diameters (Md_{ϕ} averages from −2·9 to −3·4 phi) but, as stated above, they often vary more within a single vertical profile than between different sections. Samples from the overbank deposits show an overall decrease in median diameters and an increase in sorting from the proximal deposits (only one sample with Md_{ϕ} = −6·1 phi; σ_{ϕ} = 3·9) to the re-channelled deposits (Md_{ϕ} average = −2 phi; σ_{ϕ} average = 3·8) and the interfluve deposits (Md_{ϕ} average = −1 phi; σ_{ϕ} average = 3·6). The overbank deposits from the interfluve regions plot in the same area as the marginal valley-filling deposits, implying that processes of overspilling during the 14 June events directly involved the marginal part of the channelled flow. Except for one sample, the proximal ash-cloud surge deposits are finer grained and better sorted (Md_{ϕ} average = 3 phi; σ_{ϕ} average = 1·5) than the surge deposits from the medial reaches (Md_{ϕ} average = 1·1 phi; σ_{ϕ} average = 2), demonstrating the decreasing effects of lofting and entrapment of fines from the main part of the 14 June BAFs into the overriding ash cloud by fragmentation processes that occurred mainly at each break in slope. Alternatively, progressive depletion of fine particles in the ash-cloud surge with distance from the vent may explain the variations observed.

Matrix component analysis of the deposits (Fig. 8B) shows that the proximal ash-cloud surge deposits contain more crystals and dense glass (>50 wt%) than those from the valley-filling, overbank and medial ash-cloud surge deposits (all having crystal and dense glass contents <50 wt%). The abundance of loose crystals and dense glass in the matrix of the proximal ash-cloud surge deposits is related directly to the finer grained character and better sorting of these deposits (Fig. 8A). These deposits were sampled in the proximal Gendol valley, below the first break in slope. It is suggested that the sudden change in local slope could have induced the rapid deceleration of the different flows (i.e. a hydraulic jump) and lofting of their fine particles, thus producing ash-cloud surge deposits with the observed characteristics. Some effects of fragmentation processes and abrasion of coarse clasts from the basal avalanche at the break in slope (Saucedo *et al.*, 2004) may have also contributed to fining and the abundance of loose crystals and dense glass in the proximal surge deposits. Samples from all other types of deposits show homogeneous compositions with accidental lithic contents <25 wt% and abundances of juvenile clasts between 50 and 70 wt%. However, some variations are noticeable between the different geomorphological contexts recognized. Samples from proximal valley-filling deposits have lower accidental lithic contents relative to those from medial and distal valley-filling deposits. This downflow increase in accidental lithics has also been observed at the surface of the deposits (Charbonnier & Gertisser, 2008) and is interpreted to result from a decrease in flow competence during transport, and/or flow unsteadiness conditions. Samples from the overbank deposits that were re-channelled into the surrounding valleys contain more crystals and dense glass (contents >40 wt%) than those on the interfluve area (all having contents <40 wt%). This increase in crystals and dense glass with distance from the main channel (and the overspill site) is consistent with the idea that fragmentation processes, which occurred when each flow pulse encountered the valley margins, contributed to fining and lofting of fine particles. Thus, overbank flows incorporated a greater part of the fine particles and loose crystals and dense glass and carried them away from the source.

Grain-size data of recent BAF, surge and fall deposits generated by dome collapses at Merapi, 1984 (Boudon *et al.*, 1993); Unzen, 1990 to 1995 (Miyabuchi, 1999); Colima, 1991 (Saucedo *et al.*, 2004); and Soufrière Hills, Montserrat, 26 December 1997 (Ritchie *et al.*, 2002); were chosen for comparison with data from the June 2006 BAFs of Merapi (Fig. 9). Only the 1984 deposits of Merapi are as poorly sorted as the main part of the June 2006 BAF deposits with an Inman sorting coefficient σ_{ϕ} *ca* 4. The Unzen deposits show similar median diameters and sorting to most of the 2006 overbank and marginal valley-filling deposits of Merapi; this is due to the fact that only the portion of the Unzen deposits finer than −5 phi was analysed by Miyabuchi (1999). In addition, samples from Colima and Soufrière Hills dome-collapse pyroclastic-flow deposits are better sorted and generally finer grained than those from Unzen and Merapi (Fig. 9). Even overbank and marginal Merapi deposits tend to be more poorly sorted than the Colima and Montserrat BAF deposits. The Unzen and Soufrière Hills surge deposits exhibit the greatest range of grain size and sorting, and surge samples from Colima are better sorted than

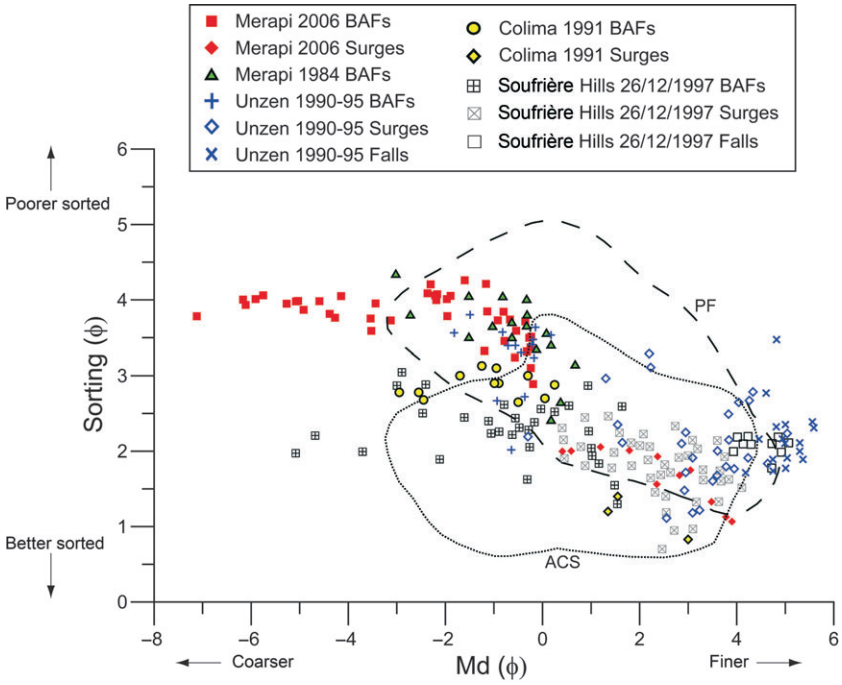

Fig. 9. Plot of median diameter ($Md_{Ø}$) versus sorting coefficient ($\sigma_{Ø}$) for BAF, surge and fall deposits produced by dome collapse from Merapi and other volcanoes. Data for the 1984 Merapi eruption are from Boudon *et al.* (1993), for the 1990 to 1995 Unzen eruption from Miyabuchi (1999), for the 1991 Colima events from Saucedo *et al.* (2004) and for the 26 December 1997 Soufrière Hills, Montserrat event from Ritchie *et al.* (2002). An explanation of the outlined areas is given in Fig. 8.

those from the 2006 eruption of Merapi. Fall deposits from Unzen and Montserrat are much finer grained than most of the surge deposits with median diameters between 4 and 6 phi. All samples from the other volcanoes presented in Fig. 9 are considered by the respective authors to be generated by simple gravitational dome collapses with a few exceptions of explosive events at Unzen in 1991. Therefore, the great variability in grain size and sorting observed between similar deposits from other volcanoes could be due to topographic factors, variations in composition of the different BAF deposits (for example, accidental lithic content, presence of pumices and/or low density clasts) fragmentation characteristics at the source (Maria & Carey, 2007; Kamata *et al.*, 2009) or a combination thereof.

Volumes of the June 2006 deposits

Eight short-runout to medium-runout (<4·5 km) BAFs generated after 14 June led to the deposition of eight overlapping lobes in the proximal and medial Gendol valley (lobes 9 to 2 on Fig. 1). The deposits are composed mainly of poorly sorted, basal avalanche material with average thicknesses of 3 to 6 m; they have volumes $<1 \times 10^6$ m^3 (Table 4) with individual lobe volumes varying from 0·08 to $0{\cdot}90 \times 10^6$ m^3. Their total deposited volume is *ca* 4×10^6 m^3 over an area of *ca* 0·36 km^2. The two long-runout (>4·5 km) BAFs generated on 14 June led to the deposition of units L1M (a.m. flow) and L1A (lobe 1, p.m. flow) and have deposit volumes $>1 \times 10^6$ m^3 (Table 4). In total, the June 2006 BAF deposits cover an area of *ca* 1·4 km^2, equally distributed between basal avalanche (35·2%), overbank (28·1%) and ash-cloud surge deposits (36·7%). Their overall volume is *ca* $8{\cdot}7 \times 10^6$ m^3, with *ca* 89% of this volume accounting for basal avalanche deposits ($7{\cdot}8 \times 10^6$ m^3), 9·2% for overbank deposits ($0{\cdot}8 \times 10^6$ m^3) and only 1·8% for ash-cloud surge deposits ($0{\cdot}15 \times 10^6$ m^3). More than half of the total volume (*ca* 54%) was deposited during the emplacement of the two major flows of 14 June. Individual lobe volumes of discrete flows generated after 14 June vary between *ca* 1·0% (for example, lobes 9 and 7) and *ca* 10% (lobe 2) of the total volume (Table 4). In contrast to all other flow deposits that are concentrated in the proximal area (between 2·0 and 3·5 km from the summit), including those from the 14 June a.m. flow, most of the deposit volume from the 14 June p.m. flow is found in the distal area between 5·8 and 6·8 km from the summit (Table 4). The volume represented by overbank deposits that were re-channelled into the surrounding valleys accounts for more than a half (*ca* 56%) of the total overbank volume emplaced during the 14 June events.

Mobility of the June 2006 block-and-ash flows

The mobility parameter ($\Delta H/L$) captures the ability of gravity driven mass flows to move

Table 4. Mobility parameters for the different BAF forming events recognized during the 2006 eruption of Merapi.

Flow	Flow type	ΔH (m)	L (m)	$\Delta H/L$	Area (m^2)	Volume (m^3)	$A/V^{2/3}$	A/L^2
14 June a.m.	BA	1790	4500	0·40	320 274	1 191 401	28·5	0·0158
14 June p.m.	BA	2070	7000	0·30	882 079	2 698 311	45·5	0·0180
Lobe 2	BA	1760	4400	0·40	278 078	900 495	29·8	0·0144
Lobe 3	BA	1695	4000	0·42	256 146	768 438	30·5	0·0160
Lobe 4	BA	1640	3700	0·44	243 779	731 337	30·0	0·0178
Lobe 5	BA	1550	3300	0·47	213 182	639 546	28·7	0·0196
Lobe 6	BA	1500	3000	0·50	186 582	559 746	27·5	0·0207
Lobe 7	BA	1430	2700	0·53	45 054	90 108	22·4	0·0062
Lobe 8	BA	1400	2600	0·54	102 327	225 818	27·6	0·0151
Lobe 9	BA	1230	2000	0·62	38 623	77 246	21·3	0·0097
Overbank K.Opak	OB	120	950	0·13	30 724	61 448	19·7	0·0340
Overbank K.Gendol 2	OB	240	1940	0·12	118 734	237 468	31·0	0·0315
Overbank K.Gendol 3	OB	130	720	0·18	30 877	61 754	19·8	0·0596

BA, basal avalanche; OB, overbank pyroclastic flow.

downslope (e.g. Hayashi & Self, 1992; Iverson, 1997). The values selected for the different 2006 BAF forming events at Merapi were calculated assuming ΔH as the difference in height between the centre of mass of the 2006 lava dome and the distal limit of each flow deposit. $\Delta H/L$ values therefore represent lower limits. $\Delta H/L$ ratios for the 2006 Merapi flows (Table 4) vary between 0·30 and 0·62. The general increase after the 14 June events, from lobe 2 to lobe 9, is related directly to the overall decrease in runout distance of these flows. The lower values (from 0·13 to 0·18) obtained for the three overbank pyroclastic flows generated on 14 June p.m. that entered the surrounding valleys compared with those of their parent flow (0·3) show that, despite their lower heights and lengths, these flows were mobile enough to inundate large areas and propagate away from the main channel confines, even on slopes well below the static angle of repose (<20°). The finer grained character of these overbank pyroclastic flows, their inherited momentum from the overspill, rapid sedimentation of their parent flow and the further channellization have certainly played a role in the enhanced mobility.

Data from recent pyroclastic flows generated by dome-collapses and fountain-collapses from: Merapi, 1998 (Schwarzkopf *et al.*, 2005); Unzen, 1991 (Yamamoto *et al.*, 1993); Colima, 1998 to 1999 (Saucedo *et al.*, 2002); Soufrière Hills, Montserrat, 1996/1997 (Calder *et al.*, 1999); and from other flow types (Fisher & Schmincke, 1984), are compared with data from the 2006 Merapi flows in Fig. 10. $\Delta H/L$ ratios obtained of the June 2006 dome-collapse pyroclastic flows are very similar to those from the 1998 BAFs at Merapi and the 1998/1999 dome-collapse and fountain-collapse pyroclastic flows at Colima, but exhibit a wider distribution. All these flows plot on the short-runout side of the small-volume pyroclastic flows from Fisher & Schmincke (1984), except for the 2006 overbank pyroclastic flows (Fig. 10). Ratios calculated for the latter are even lower than those found from the 1991 BAFs at Unzen and the dome-collapse and fountain-collapse pyroclastic flows from the 1996/1997 period at Soufrière Hills, Montserrat; however, they have similar ratios to those from the secondary pyroclastic flows derived from the largest events on 25 June and 26 December 1997 at Montserrat. Similar factors (i.e. fine-grained nature, rapid sedimentation from the dilute suspensions and channellization) were invoked by Calder *et al.* (1999) to explain the enhanced mobility of these secondary flows. Following work by Dade & Huppert (1998) and Calder *et al.* (1999) on the mobility of different kinds of pyroclastic density currents at Soufrière Hills, the results are considered in terms of the geometric parameter $A/V^{2/3}$ and the plan-shape parameter A/L^2 (Table 4). Compilation of cold rock avalanches and surges from elsewhere (Howard, 1973; Lucchitta, 1978, 1979; Voight, 1978; Crandell *et al.*, 1984; Francis *et al.*, 1985; Siebert *et al.*, 1987; McEwen & Malin, 1989; Stoopes & Sheridan, 1992) were added for comparison (Fig. 11). Integration of the new data for BAF forming events at Merapi in 2006, and at Colima in 1998/1999, suggests that the aspect ratios $A/V^{2/3}$ of dome-collapse pyroclastic flows are similar to those obtained for Soufrière Hills and cold rock avalanches, and that the aspect

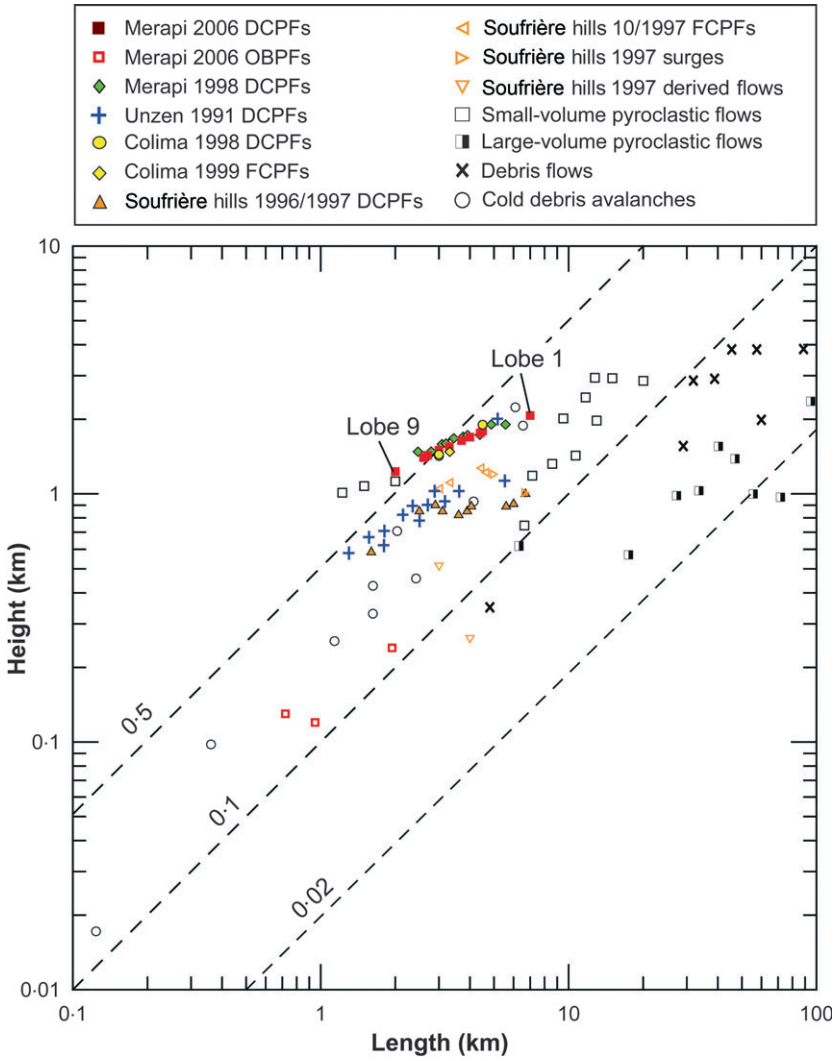

Fig. 10. Vertical drop (ΔH) and horizontal travel distance (L) ratios for the June 2006 pyroclastic flows of Merapi in comparison with those from Merapi, 1998 (Schwarzkopf *et al.*, 2005); Unzen, 1991 (Yamamoto *et al.*, 1993); Colima, 1998 to 1999 (Saucedo *et al.*, 2002); Soufrière Hills, Montserrat, 1996/1997 (Calder *et al.*, 1999); and from other flow types (Fisher & Schmincke, 1984). DCPFs, dome-collapse pyroclastic flows; OBPFs, overbank pyroclastic flows; FCPFs, fountain-collapse pyroclastic flows; Derived Flows, surge derived flows.

ratios $A/V^{2/3}$ of the different types of density currents are almost independent of their volumes (Fig. 11B). The three overbank pyroclastic flows from Merapi have aspect ratios similar to their parent flows (Fig. 11A and B) but higher plan-shape ratios A/L^2 (Fig. 11C). In fact, overbank pyroclastic flows can be considered more mobile than their parent flows only when the runout distance is included into the characterization of flow mobility. A/L^2 is equivalent to the ratio of the average width to the length of an avalanche deposit. Therefore, A/L^2 values for the Merapi overbank flows of 0·03 to 0·05 correspond to a radial spread of <10°, similar to the Montserrat dome-collapse flows, but significantly lower than the 120° found for large, non-volcanic rockfalls and debris avalanches (Dade & Huppert, 1998).

Calder *et al.* (1999) suggest that the channellization of small flows could result in lower values of the plan-shape ratio A/L^2. These authors also propose that topographic factors were partly the cause of the considerable scatter seen in the mobility ratios of the different types of pyroclastic flows included in their study. The effect of terrain on smaller flows is likely to be considerably greater; this is particularly valid for volcanoes, with eruptive activity characterized by the formation and subsequent destruction of a lava dome at the summit of a high and steep-sloped cone (for example, Soufrière Hills, Merapi and Unzen). The high relief of such volcanoes leads to the formation of deep channels on the middle to lower flanks. As a result, the presence of these channels is likely to have a significant control on the behaviour of pyroclastic flows and the distribution of their deposits. The differences in the mobility between the different types of pyroclastic flows may, to some extent, also relate to the mode of formation and material properties, and a variable role of gas fluidization (Calder *et al.*,

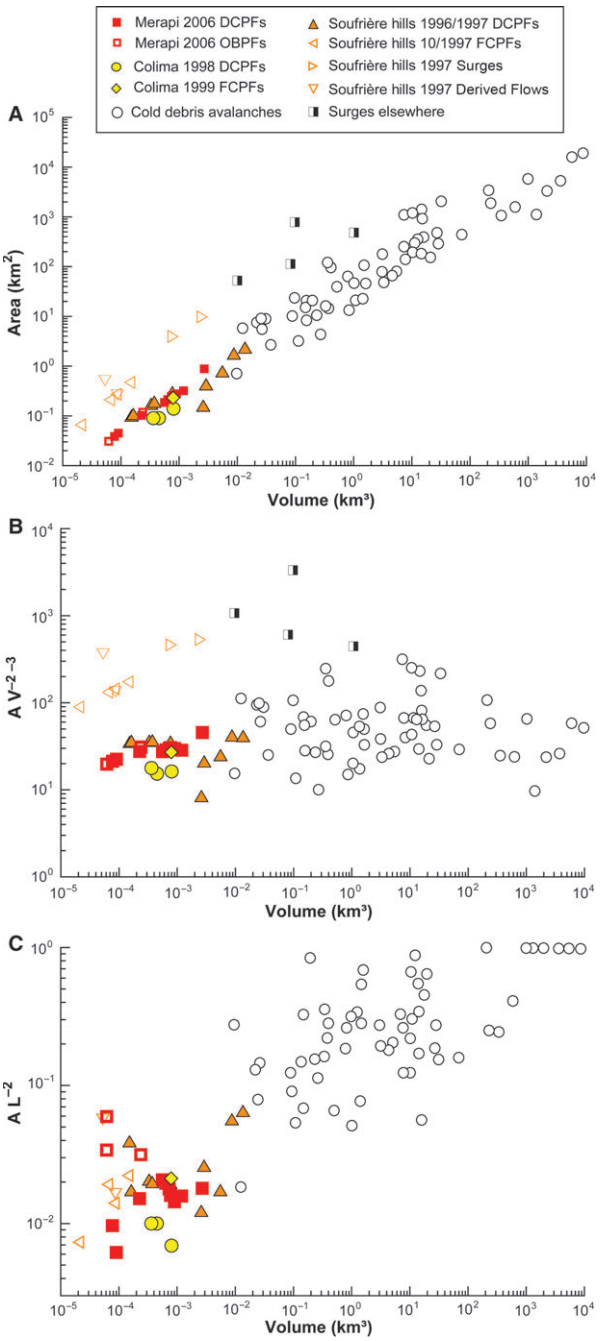

Fig. 11. Plots of: (A) the area inundated; (B) the mobility ratio $A/V^{2/3}$; and (C) the plan aspect ratio A/L^2 as functions of flow volume V for the different kinds of pyroclastic flows on Merapi, Colima and Soufrière Hills, Montserrat and cold rock avalanches and pyroclastic surges known from elsewhere. Data compiled from: Howard (1973), Voight (1978), Lucchitta (1978, 1979), Crandell *et al.* (1984), Francis *et al.* (1985), Siebert *et al.* (1987), McEwen & Malin (1989), Stoopes & Sheridan (1992), Calder *et al.* (1999) and Saucedo *et al.* (2002). DCPFs, dome-collapse pyroclastic flows; OBPFs, overbank pyroclastic flows; FCPFs, fountain-collapse pyroclastic flows; Derived Flows, surge derived flows.

1999). The progressive filling of the Gendol valley between half and two-thirds of its total depth by previous flows during early June 2006 at Merapi (Charbonnier, 2009) may have also played a role for the evolution of the 14 June BAFs and their tendency to overbank.

Results from the mobility of the June 2006 BAFs at Merapi show that there is a scale dependence of the runout behaviour of BAFs based on whether they are large enough to exceed a threshold determined by the topography of the receiving landscape, at which point they can undergo a flow transformation that enables a different kind of flow-type to emerge (i.e. overbank flows) with greater mobility and, hence, hazard potential. Therefore, the transport and emplacement mechanisms proposed for these flows need to be able to account for the observed mobility characteristics.

Conceptual models of transport and deposition of the June 2006 block-and-ash flows

Two main types of BAFs (short-runout to medium-runout BAFs and long-runout BAFs) are distinguished in this paper, based on the parameters discussed in the previous sections. Table 5 summarizes these parameters, as well as the characteristics of the deposit morphology and components that are utilized to develop conceptual models, based on longitudinal and lateral deposit variations. In this way, the facies identified in the June 2006 deposits provide a view inside various parts of the frozen state of each flow, demonstrating the effects of changing slope, channel morphology and local topographic features on flow dynamics. The two models are illustrated by capturing the flow and deposition mechanisms of the two types of BAFs at selected 'observation points' along the southern flank of the volcano.

Short-runout to medium-runout block-and-ash flows

The model presented in Fig. 12 is based mainly on a detailed study of the lobate deposits of the short-runout to medium-runout BAFs that were emplaced after 14 June 2006 at Merapi. Position P1 captures the flow just after its generation during a relatively short (<1 min) and discrete dome-collapse event with a collapsed volume $<1 \times 10^6$ m^3. The motion is governed by flow acceleration on the unconfined upper flanks with steep slopes >30°, which corresponds to the erosional stage of a quasi-steady to unsteady

Table 5. Summary of observations of the 2006 block-and-ash flows at Merapi based on results obtained during this study.

	Short-runout to medium-runout block-and-ash flows	Long-runout block-and-ash flows
Generation mechanisms	Short and discrete (<1 min) dome-collapse events	Sustained (tens of mins), multiple-pulses (2 to 10) dome-collapse events
Area covered	<300 000 m^2	>300 000 m^2
Deposited volume	$<1 \times 10^6$ m^3	$>1 \times 10^6$ m^3
Runout distance	<4 km	>4 km
Slopes of deposition	*ca* 20°	<20°
Velocity	15 to 30 m s^{-1}	15 to 45 (25 to 60 for surges) m s^{-1}
Mobility parameters	$\Delta H/L$: 0·4 to 0·6 $A/V^{2/3}$: 20 to 30 A/L^2: 0·01 to 0·02	$\Delta H/L$: 0·3 to 0·4 (0·1 to 0·2 for overbank flows) $A/V^{2/3}$: *ca* 45 (*ca* 20 for overbank flows) A/L^2: 0·02 (0·03 to 0·06 for overbank flows)
Transport mechanisms	Quasi-steady to unsteady granular flow	Unsteady, cohesionless grain flows with inertial flow regime
Deposition mechanisms	Similar to granular-free surface flow on unconfined planes	Stepwise aggradation of granular-dominated pulses
Flow types	Basal avalanche	Basal avalanche, overbank flows, ash-cloud surges
Associated deposits	Valley-filling	Valley-filling, overbank, surge
Deposit morphology	Unconfined	Confined with overbanking
Lithology	>80% juvenile clasts, outer part of the lava dome	Accidental lithic content increases downstream Overbank deposits enriched in low-density clasts
Granulometry	Bimodal distribution, poorly sorted ($\sigma_Ø$ from 3·8 to 4), $Md_Ø$ from −5 to −1, ash content from 40 to 55 wt%	Polymodal distribution, poorly sorted ($\sigma_Ø$ from 2·9 to 4·2), $Md_Ø$ from −3·5 to −0·2, ash content from 40 to 70 wt%
Seismic signal	Single pulse <3 min	Multiple pulses >3 min

granular pyroclastic density current. As the flow moves downslope, grain interactions and fragmentation processes develop a sufficient granular temperature to induce segregation processes such as kinetic sieving (Middleton, 1970; Savage & Lun, 1988) and kinematic squeezing (Le Roux, 2003) of the largest particles. No deposition occurs and erosion of the basement surface leads to the incorporation of accidental lithic clasts into the basal portion of the flow (Fig. 12). Upward gas flow generated by the fragmentation processes at the flow centreline is responsible for the formation of an ash cloud, accompanying, sheared by and pulled downslope by the basal avalanche (type 2 ash-cloud surges of Saucedo *et al.*, 2004).

After a long and steep decline, position P2 corresponds to the passage of the flow at the first break in slope, where the most proximal BAF deposits were found (Figs 2 and 12). Erosive power of the flow strongly decreased with constantly decreasing slopes and neither erosion nor deposition occur before the break in slope. Rapid flow deceleration at the break in slope induces a sudden increase in grain interlocking and frictional forces at the base of the current. However, the velocity of the flow front at the centreline is still too high for deposition,

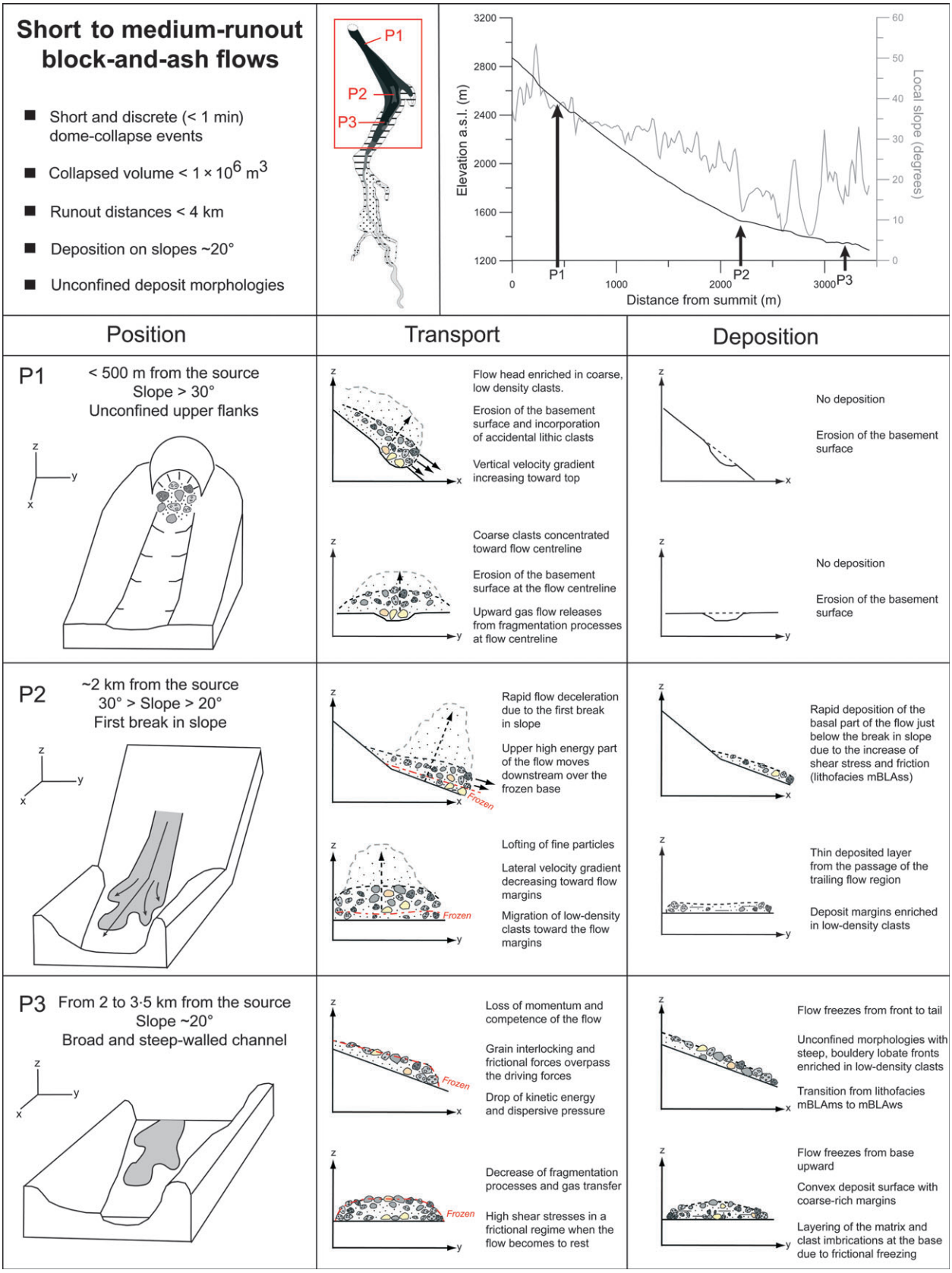

Fig. 12. Conceptual model of transport and deposition for short-runout to medium-runout BAFs from the 2006 eruption of Merapi. See text for explanation.

producing a decrease in the lateral velocity gradient towards the flow margins. As a result, the upper and frontal high-energy part of the flow moves downstream over the already frozen base and low-density clasts migrate toward the flow margins. Rapid freezing of the basal and trailing regions of the flow immediately below the break in slope leads to the deposition of a thin, coarse-clast depleted layer (Fig. 12). The change in slope also enhances turbulence with the lofting of fine particles and upward development of an ash cloud. In this case, its bulk density is less than the surrounding ambient fluid and it lofts convectively and stops.

Position P3 is characteristic for the depositional stage of a decelerating flow on slopes below the angle of repose for dry pyroclastic material (*ca* 20°). Here, the presence of a broad and steep-walled channel and absence of any lateral confinement lead to a rapid spreading and thinning of the flow. Progressively, grain interlocking and frictional forces overcome the driving forces and kinetic energy, and the dispersive pressure inside the flow drops. The flow freezes rapidly from the base upwards and from front to tail, and high shear stresses in a frictional regime occur at the time of deposition. The associated deposits show unconfined morphologies with steep, boulder and lobate fronts that are enriched in low-density clasts. Layering of the matrix due to frictional freezing and sheet-like termination facies are also common features observed with a sudden loss of momentum and competence of the flow just after a break in slope (lithofacies mBLAms of unit L6 at section CS1, Fig. 2).

Long-runout block-and-ash flows

The model for long-runout BAFs (Fig. 13) is based on a detailed study of the 14 June 2006 BAFs at Merapi and integrates current models of transport and deposition mechanisms of small-volume pyroclastic density currents (e.g. Schwarzkopf *et al.*, 2005; Lube *et al.*, 2007; Sulpizio *et al.*, 2007). Position P1 (Fig. 13A) captures the flow just after the beginning of a sustained (tens of minutes), multiple-pulse (2 to 10 pulses) dome-collapse event that involves material from the inner part of the lava dome. Successive generation of closely spaced dome collapses generates a total collapsed volume that typically exceeds 1×10^6 m^3. After only tens of seconds, the first major flow pulse accelerates on the unconfined upper flanks with steep slopes >30°; this corresponds to a flow regime where the gravitational forces largely overcome the resistance forces. High velocities of the flow head enriched in coarse, low density clasts lead to erosion of the substrate and incorporation of accidental lithic clasts during its passage, the amount of which increases with each new flow pulse. Strong upward and lateral gas flow generated by fragmentation processes at the flow centreline result in rapid vertical and lateral spreading of the main body of the flow. An overriding cloud of gas and fine particles also expands laterally and masks the progression of the underflow. At this early stage of transport, the flow is interpreted to move downslope as independent pulses that are not connected with each other yet; its pulsating behaviour is only controlled by variations of the material released at the source. No deposition from the main flow body occurs, but thin lapilli–ash layers are often observed on margins due to the rapid settling of the marginal parts of the accompanying ash-cloud surge (Fig. 13A).

Position P2 marks the passage of the flow at the first break in slope that also corresponds, in this case, to the transition from an unconfined to a confined depositional area (Fig. 13A). Rapid deceleration of each flow pulse at the break in slope induces a sudden increase in grain interlocking and frictional forces from its base. However, grain interactions and fragmentation processes develop a sufficient granular temperature to induce segregation processes such as kinetic sieving and kinematic squeezing of the largest particles. Moreover, the high velocities of the flow-pulse fronts at the centreline with similar characteristics to the flow head inhibit deposition, producing a decrease in the lateral velocity gradient towards the flow-pulse margins. As a result, the upper and frontal high-energy part of each pulse moves downstream over the already frozen base and low-density clasts migrate towards the flow-pulse margins. Deposition occurs stepwise, with rapid aggradations of stacked sub-units from frozen basal and marginal parts of granular-flow-dominated pulses, that is, in some respects, similar to the depositional model of Sulpizio *et al.* (2007). Field evidence for these mechanisms include levées and channel deposits, with valley-filling deposits depleted in coarse clasts and marginal deposits enriched in low-density clasts (unit L1A in Fig. 2; Tables 2 and 3), and inverse coarse-tail grading, with clast trains at the top of each sub-unit (association of lithofacies mBLAss in unit L1A at section CS1, Fig. 2). The apparent lack of erosive surfaces and/or deposition of fine ash between the stacked sub-units suggests that the different pulses are the

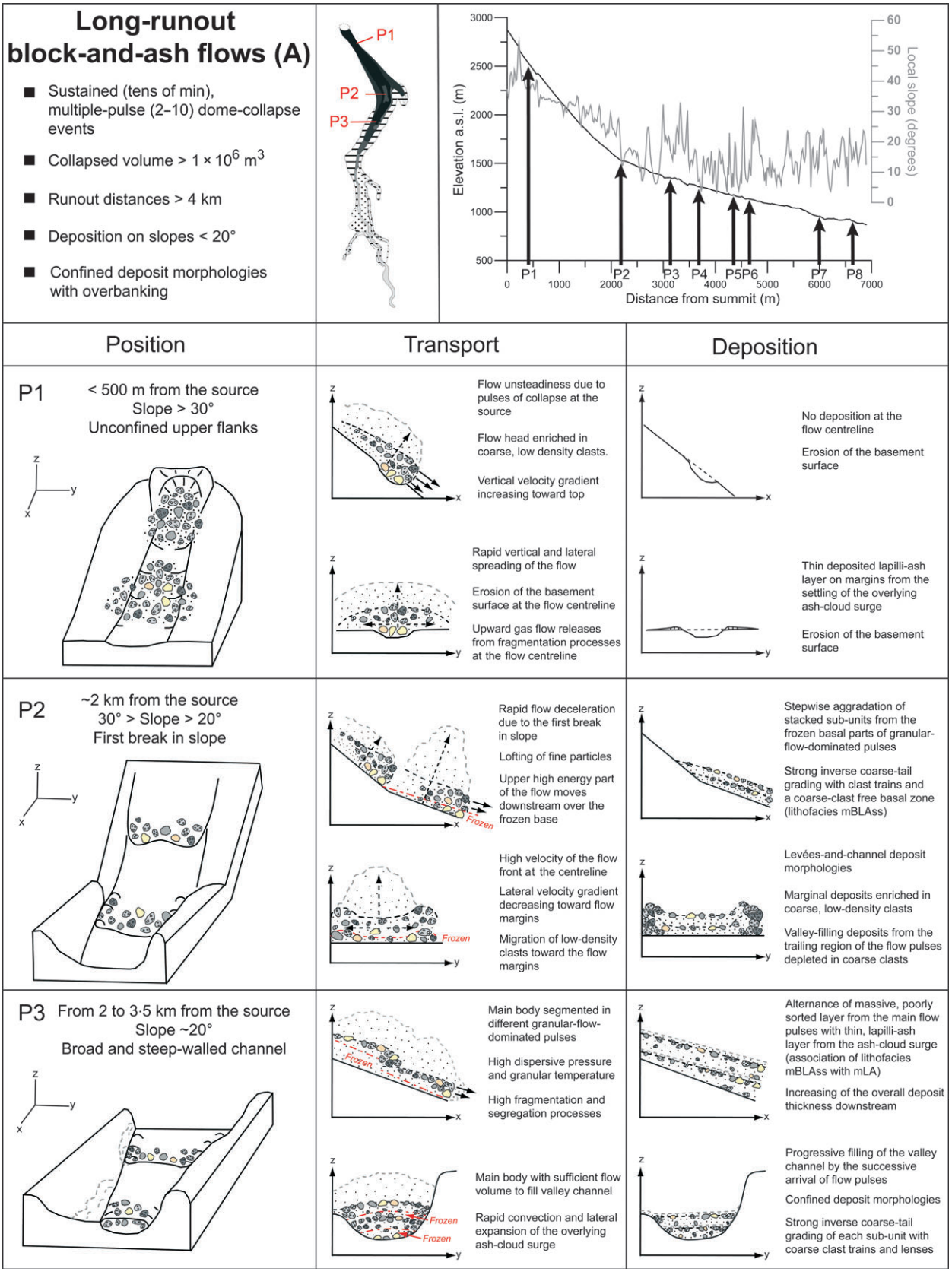

Fig. 13. Conceptual model of transport and deposition for long-runout BAFs from the 2006 eruption of Merapi in the: (A) proximal area; (B) medial area; and (C) distal area. See text for explanation.

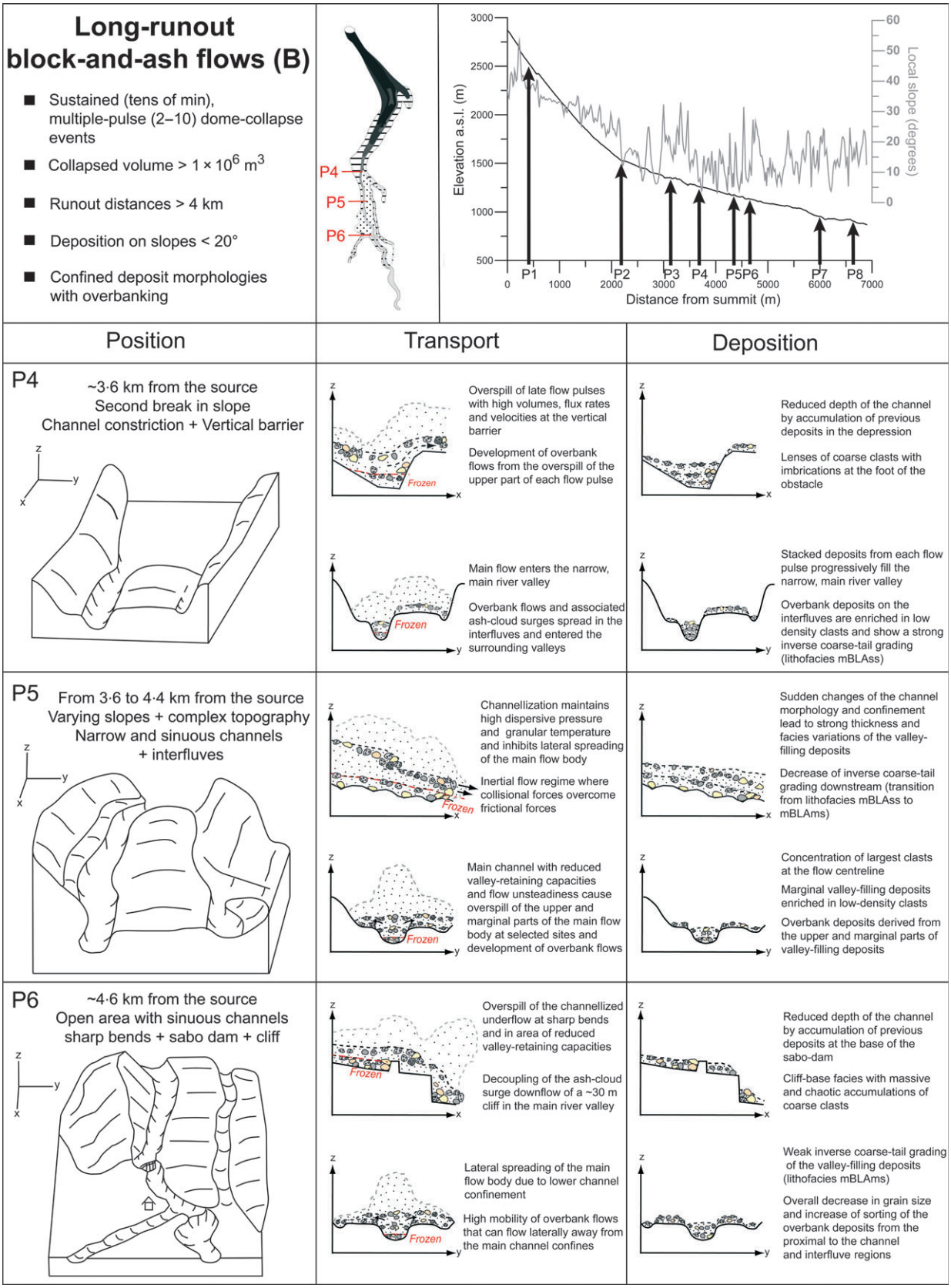

Fig. 13. (*Continued*)

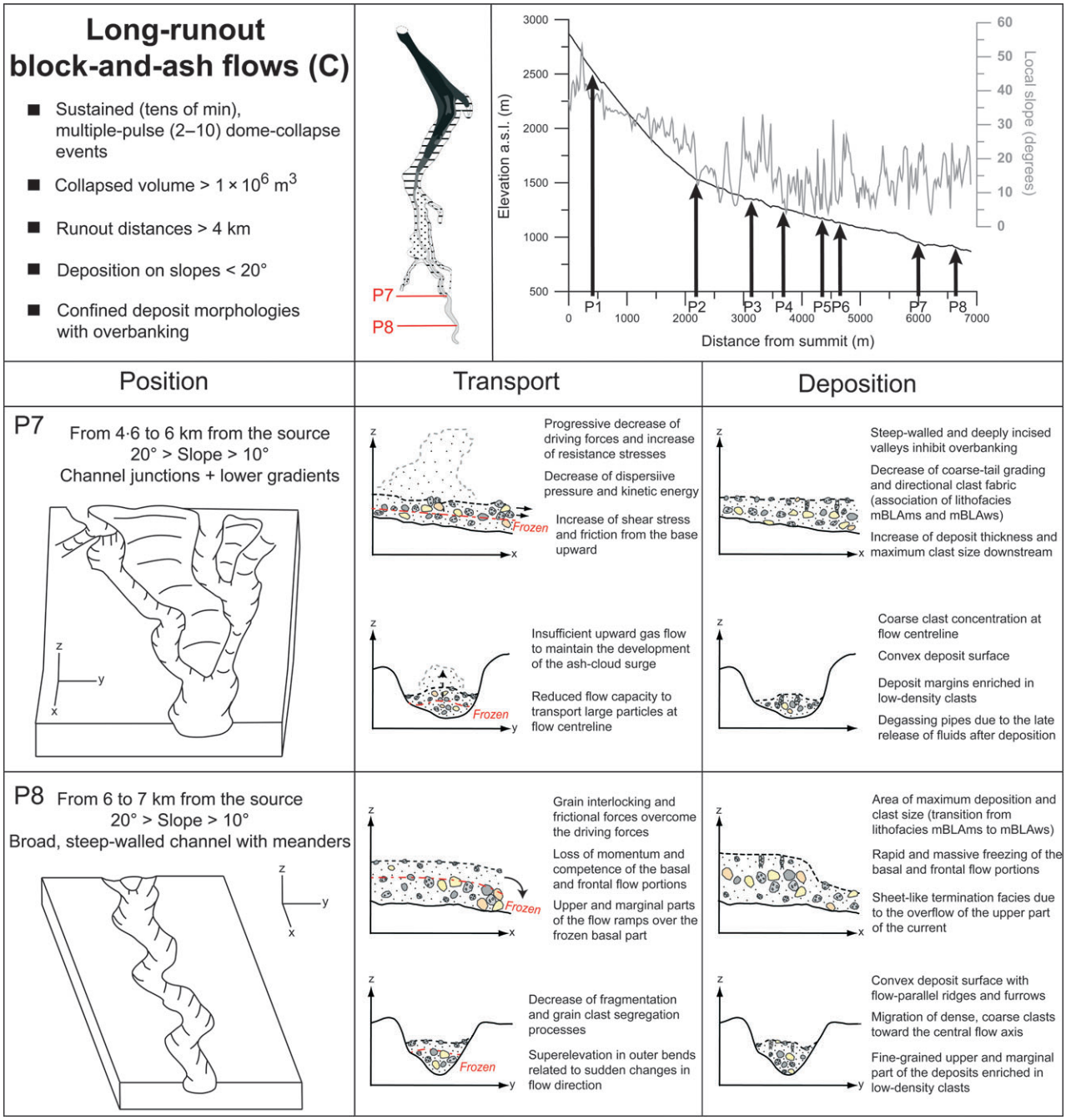

Fig. 13. (*Continued*)

result of heterogeneous mass distribution within the current rather than variations of material released at the source. In contrast to short-runout to medium-runout BAFs, a higher degree of fragmentation inside the main flow body induces the generation of a sufficient volume of ash and deposition of a massive, fine-grained and well-sorted lapilli–ash layer on top of the deposit sequence (lithofacies mLA and mA in unit S1A, Fig. 2).

Position P3 represents flow transport and deposition in a proximal valley with a constant slope (*ca* 20°) and a single broad and steep-walled channel that narrows progressively downstream (Fig. 13A). In contrast to the short-runout to medium-runout BAFs at the same location, the main flow body has a sufficient initial volume to fill the valley channel. The progressive increase in channel confinement plays a key role in maintaining a high dispersive pressure and

granular temperature, and inhibiting further lateral spreading and thinning of the flow. The flow regime in this area is interpreted as inertial where collisional forces largely overcome frictional forces. The flow moves downslope as an unsteady, cohesionless grain flow in which the momentum is transferred between clasts during frequent collisions. Flow unsteadiness causes the main body of the flow to be segmented into different pulses that run very close to each other (Fig. 13A). Deposit facies associations such as the alternation of massive, poorly sorted and reversely graded layers with thin, well-sorted lapilli–ash layers are further evidence for the stepwise aggradations of discrete pulses (association of lithofacies mBLAss with mLA at section CS5, Fig. 2). Successive arrival of flow pulses progressively fills the valley channel and increases the overall deposit thickness. The change in slope could have enhanced turbulences with the lofting of fine ash produced during the passage of the first pulse and its partial entrapment by the following pulse, producing the lithofacies associations observed (units L1A and S1A at section CS5, Fig. 2). The presence of marginal, fine-grained lapilli–ash deposits on the outer banks of the valley indicates ash elutriation due to rapid convection and lateral expansion of a highly mobile ash-cloud surge (type 1 ash-cloud surge of Saucedo *et al.*, 2004). Further evidence for the detachment of the dilute, more mobile upper part of the flow in such an area includes rapid local variations of the singe zone on valley walls and surge effects on the vegetation (Charbonnier, 2009).

Position P4 (Fig. 13B) captures the flow at the second break in slope, characterized by the presence of a channel constriction and a vertical barrier (old terrace that faces the flow). When the flow reaches this point, its dynamics consist of high velocities and energy of the main body and increasing volume and thickness due to the successive arrival of individual pulses closely spaced in time. The combined effects of constriction of the topographic channel and reduction in cross-sectional area by previous accumulation of pyroclastic deposits at the base of the vertical barrier causes the upper part of the following flow pulses to bank up, thicken and leave the channel at this particular location. Only the overspill of late flow pulses with higher volumes, flux rates and velocities lead to the development of overbank flows and associated surges that spread onto the interfluves and enter the surrounding valleys. Due to the fine-grained nature of their deposits and abundance of low-density clasts, overbank flows are derived from the upper and marginal parts of each flow pulse (unit OB1, Fig. 5). The great thickness of the valley-filling deposits and the presence of stacked sub-units with lenses/imbrications of coarse clasts at the foot of the obstacle (units L1M and L1A at section CS5, Fig. 2) suggest that most of the material did not leave the channel at this point and entered the narrow and sinuous segment of the main river valley. This interpretation is corroborated by the presence of a single, reversely graded unit in the overbank deposits that lies on the top of the terrace with a limited volume and area covered (lithofacies mBLAss in unit OB1 at section IN1, Fig. 5).

Position P5 shows the progression of the flow in the medial area that exhibits a complex topography with varying slopes and sudden changes in channel morphology and confinement (Fig. 13B). Channel confinement helped the flow to keep a relatively high energy and velocity and preserved some of the depositional features observed in the proximal area. Reduced valley-retaining capacities of the narrow and sinuous main river valley and flow unsteadiness with stages of acceleration and deposition controlled the ability of the flow to overspill the valley margins at selected sites. In areas of decreasing slopes, lower channel confinement and higher sinuosity, the arrival of each flow pulse front increases the potential of overbanking of the upper and marginal parts of the main flow body. In these areas, grain dispersive pressure and clast segregation dropped more rapidly near the central flow axis, causing the migration of coarse particles towards the channel centre. Lateral deposit facies variations include maximum thickness and concentration of the largest clasts near the flow centreline and enrichment in low-density clasts, finer grained nature and lack of any grading of the marginal valley-filling deposits (units L1M and L1A at sections CS6 to CS9, Fig. 3). Coarse-tail reverse grading and development of a lower coarse-clast free basal zone in each sub-unit, flow alignment of clast long axes and zones of clast imbrications support a flow regime where particle collisions were encouraged and resulting grain-dispersive pressures and processes of density clast segregation were extremely high (lithofacies mBLAss in unit L1A at sections CS6 to CS9, Fig. 3). These valley-filling deposit characteristics tend to disappear progressively downstream when the flow entered open areas with lower gradients.

Position P6 corresponds to the passage of the flow in an open and broad area composed of narrow and sinuous channels and flat interfluves (Fig. 13B); this is also the typical location for the first settlements on the interfluves. Significant changes in valley morphology and channel gradients occur along the flow path, including the presence of a sharp bend and a cliff inside the main channel. The construction of a sabo dam structure just after a sharp bend, intended as a preventive measure against lahars, has also contributed to reduction of the depth of the main channel by accumulation of earlier deposits at the base (Fig. 13B). The presence of a flow with high energy and strong potential for superelevation in a narrow and sinuous channel increases the risk of lateral spreading and overbanking of the main flow body when a sudden change in the channel morphology occurs. Overspill of the channelled underflow typically is observed at sharp bends and in areas of reduced valley-retaining capacities (for example, presence of a sabo dam structure). Voluminous and highly mobile overbank flows produced by overspill of the upper and marginal parts of the main flow pulses can flow laterally away from the main channel confines, spread onto interfluves and partially fill the surrounding valleys (Fig. 13B). Three main depositional zones are recognized for the overbank deposits. Decrease in grain size and increase in sorting occur from the proximal (wedge-shaped) to the channel and interfluve regions (unit OB1 at sections KA1 to KA3, Fig. 5). Each of these depositional zones is composed of poorly sorted and reversely graded sub-units resulting from rapid deposition of successive flow pulses during overspill of a single, sustained current (association of lithofacies mBLAss with mBLAms in unit OB1 and OB2 at sections KA1, KA2 and IN3, Fig. 5). Facies correlations between valley-filling and overbank deposits show that the arrival of each flow pulse front at a given site in the main river valley controls the generation of overbank flow pulses on the interfluves. The presence of a cliff in the main river channel also affects flow transport and deposition. At this location, due to the sudden loss of topographic control, the ash cloud decouples from the basal avalanche and spreads laterally beyond the valley walls (Fig. 13B). The channelled underflow suddenly loses its flow character and deposits characterized by massive and chaotic accumulations of coarse clasts, similar to the cliff-base facies (Schwarzkopf *et al.*, 2005) are observed below the cliff.

Position P7 is characteristic for flow and deposition in steep-walled and deeply incised valleys with slopes below the static angle of repose (Fig. 13C). In this region, channel junctions are likely to occur and channels generally become broader and deeper. As the channel gradients become lower and channellization decreases, driving forces progressively decrease while resistance stresses increase during flow motion from the base upwards. Particle collisions become more subdued due to a decrease in kinetic energy and grain dispersive pressure as the flow moves downslope, although it is still strong enough to orient particle long axes. The progressive reduction in clast fragmentation below a certain threshold inside the main flow body induces insufficient upward gas flow to maintain the presence of a dilute ash-cloud surge that progressively becomes cooler and slower downstream (Charbonnier & Gertisser, 2008). Overbanking generally is inhibited by broad and steep-walled channels but can occur locally inside the main river valley when flows pass round bends or beyond channel constrictions. The absence of sub-units with coarse-clast trains in the channelled deposits (lithofacies mBLAws in unit L1A at sections CS12 to CS17, Fig. 4) suggests that only major flow pulses with sufficient momentum and energy are able to reach distal areas. The overall increase in deposit thickness and maximum clast size downstream reflects the progressive increase in material supply from the current through the lower flow boundary (Branney & Kokelaar, 2002). Concave and flat deposit surfaces are progressively replaced downstream by convex surfaces (Charbonnier & Gertisser, 2008), with concentration of coarse clasts toward the channel centre and finer grained upper and marginal deposits enriched in low-density clasts (unit L1A at sections CS13, CS14 and CS15, Tables 2 and 3). The presence of degassing pipes in the upper, finer grained part of the valley-filling deposits (unit L1A at section CS16, Fig. 4) indicates the late release of fluids after deposition (Branney & Kokelaar, 2002).

Position P8 illustrates flow and deposition behaviour in a distal, broad and steep-sided channel with meanders (Fig. 13C). As the flow enters still broader channel reaches and lower gradients, grain interlocking and frictional forces overcome the driving forces, while fragmentation and clast segregation processes progressively decrease. This area is the typical location of maximum deposition and clast size (lithofacies mBLAms in unit L1A at section CS16, Fig. 4).

Rapid flow deceleration, together with a sudden reduction in the capacity of the flow to transport large particles just before it comes to rest, results in massive and rapid freezing of the basal and frontal, coarser regions of the flow. Typical deposit facies, such as the lack of any grading, clast directional fabric and/or sub-units in the main deposit body, are further evidence for *en masse* deposition of the basal and frontal flow regions (lithofacies mBLAws in unit L1A at section CS17, Fig. 4). Several meanders in the flow path further upstream could have helped the upper and marginal regions of the flow with higher mobility to move independently from the basal and central parts and to rise up the outside of bends. Due to its lower velocity and greater mass, the main part of the flow would have been deposited first, rapidly followed by the later, less dense, overflowing part. A convex deposit surface with flow-parallel ridges and furrows and a sheet-like termination facies (Charbonnier & Gertisser, 2008) further support a model of deposition mechanisms involving rapid energy loss of the basal and central portions of the flow by frictional freezing and/or overflow of its upper and marginal parts.

CONCLUSIONS

Variations in the distribution, surface morphology and lithology of the 2006 Merapi block-and-ash flow (BAF) deposits are related to the source materials involved during individual BAF forming events and to the effects of changing slope, channel morphology and local topographic features on flow dynamics. Detailed studies of the BAF deposits emplaced on 14 June 2006 and their lateral and longitudinal facies variations provide a complete record of the consecutive transport and depositional stages that occurred during the generation of a sustained, multiple-pulse dome-collapse event. Results emphasize the potential hazard of long-runout, voluminous BAFs at Merapi through the recognition of overbank pyroclastic flows. Due to their potential to spread across densely populated interfluve (non-valley) regions, these overbank flows are considered as one of the most hazardous parts of the BAF system.

Two main types of BAFs (short-runout to medium-runout BAFs and long-runout BAFs) are recognized based on parameters including generation mechanism, flow volume, travel distance, deposit morphology, distribution, lithology and grain-size distribution. Comparison with published data from other BAFs has shown that the influence of topography and/or variations in source materials are likely to have a significant control on the mobility of BAFs and the distribution of their deposits. In particular, the finer grained character of overbank pyroclastic flows, their inherited momentum from the overspill, rapid sedimentation of their parent flow and further channellization have played a role in their enhanced mobility.

Transport and depositional mechanisms of the two types of BAFs identified have been examined through the development of two conceptual models. Variations in runout distances observed for short-runout to medium-runout BAFs (from 2 to 3·5 km for the 2006 BAFs) are linked directly to varying initial flow volumes, degrees of fragmentation and material properties of the moving mass during transport, with the largest and finer grained flows having the greatest mobility. However, deposition occurs only over a narrow range of basal inclinations that are close to the angle of repose for pyroclastic material (between 20 and 30°), indicating that such flows at Merapi behave in a similar way to granular-free surface flows on unconfined planes. Flow mechanisms of long-runout BAFs at Merapi are interpreted to be similar in many respects to unsteady, cohesionless grain flows with an inertial flow regime where collisional forces largely overcome frictional forces. Flow unsteadiness (either from a series of retrogressive dome failures and/or inhomogeneous mass distribution within the current) causes the main body to be segmented into different pulses that run closer to each other as the flow moves downslope. Block-and-ash flow deposition occurs stepwise, with rapid aggradation of stacked sub-units from different parts of the major flow pulses. In such a model, the arrival of each flow pulse front at selected sites in the main river valley controls the generation and development of highly mobile, unconfined pyroclastic flows outside valley regions and associated overbank deposits.

ACKNOWLEDGEMENTS

SJC thanks Peter Styles (Keele University), The Geological Society of London and The International Association of Sedimentologists for financial support for fieldwork in Indonesia. We also thank Antonius Ratdomopurbo (Earth Observatory of Singapore) and Subandrio (Center of

Volcanology and Geological Hazard Mitigation at the Merapi Volcano Observatory, Yokyakarta) for discussions about the 2006 Merapi eruption. Further thanks go to Vern Manville and Roberto Sulpizio for their helpful and constructive comments.

REFERENCES

Abdurachman, E.K., Bourdier, J.L., Voight, B. and **Kelfoun, K.** (2000) Nuées ardentes of 22 November 1994 at Merapi Volcano, Indonesia. *J. Volcanol. Geotherm. Res.*, **100,** 345–361.

Allen, S.R. and **Cas, R.A.F.** (1998) Rhyolitic fallout and pyroclastic density current deposits from a phreatoplinian eruption in the eastern Aegean sea, Greece. *J. Volcanol. Geotherm. Res.*, **86,** 219–251.

Bagnold, R.A. (1954) Experiments on a gravity-free dispersion of large solid spheres in a Newtonian fluid under shear. *Proc. Royal Soc., London, A*, **225,** 49–63.

BGVN. (2007) *Bulletin of the Global Volcanism Network*. Smithsonian Institution, Washington, DC, **4,** 32–2.

Blott, S.J. and **Pye, K.** (2001) GRADISTAT: a grain size distribution and statistics package for the analysis of unconsolidated sediments. *Earth Surf. Processes Land.*, **26,** 1237–1248.

Boudon, G., Camus, G., Gourgaud, A. and **Lajoie, J.** (1993) The 1984 nuée ardente deposits of Merapi volcano, Central Java, Indonesia: stratigraphy, textural characteristics, and transport mechanisms. *Bull Volcanol.*, **55,** 327–342.

Bourdier, J.-L. and **Abdurachman, E.K.** (2001) Decoupling of small-volume pyroclastic flows and related hazards at Merapi volcano, Indonesia. *Bull. Volcanol.*, **63,** 309–325.

Branney, M.J. and **Kokelaar, B.P.** (2002) Pyroclastic density currents and the sedimentation of ignimbrites. *Geol. Soc. Lond. Mem.*, **27,** 143.

Calder, E.S., Cole, P.D., Dade, W.B., Druitt, T.H., Hoblitt, R.P., Huppert, H.E., Ritchie, L., Sparks, R.S.J. and **Young, S.R.** (1999) Mobility of pyroclastic flows and surges at the Soufrière Hills Volcano, Montserrat. *Geophys. Res. Lett.*, **26,** 537–540.

Cas, R.A.F. and **Wright, J.V.** (1987) *Volcanic Successions*. Chapman & Hall, London, 528 pp.

Charbonnier, S. (2009) The dynamics and hazards of small-volume pyroclastic flows: a case study of the 2006 eruption of Merapi volcano, Java, Indonesia. PhD Dissertation, Keele University, United Kingdom, 347 pp.

Charbonnier, S. and **Gertisser, R.** (2008) Field observations and surface characteristics of pristine block-and-ash flow deposits from the 2006 eruption of Merapi Volcano, Java, Indonesia. *J. Volcanol. Geotherm. Res.*, **177,** 971–982.

Cole, P.D., Guest, J.E. and **Duncan, A.M.** (1993) The emplacement of intermediate volume ignimbrite: a case study from Roccamonfina volcano, southern Italy. *Bull Volcanol.*, **55,** 467–480.

Crandell, D.R., Miller, C.D., Glicken, H., Christiansen, R.L. and **Newhall, C.G.** (1984) Catastrophic debris avalanche from ancestral Mount Shasta volcano, California. *Geology*, **12,** 143–146.

Dade, W.B. and **Huppert, H.E.** (1998) Long runout rockfalls. *Geology*, **26,** 803–806.

Dellino, P., Zimanowski, B., Buettner, R., La Volpe, L., Mele, D. and **Sulpizio, R.** (2007) Large scale experiments on the mechanics of pyroclastic flows: design, engineering and first results. *J. Geophys. Res.*, **112,** B04202.

Doyle, E.E., Hogg, A.J., Mader, H.M. and **Sparks, R.S.J.** (2010) A two-layer model for the evolution and propagation of dense and dilute regions of pyroclastic currents. *J. Volcanol. Geotherm. Res.*, **190,** 365–378.

Druitt, T.H. (1992) Emplacement of the 18 May 1980 lateral blast deposits east-northeast of Mount St Helens, Washington. *Bull Volcanol.*, **54,** 554–572.

Druitt, T.H. (1998) The eruption, transport and sedimentation of pyroclastic flows. In: *The Physics of Volcanic Eruptions* (Eds J. Gilbert and R.S.J. Sparks), *Geol. Soc. Lond. Spec. Publ.*, **145,** 147–200.

Fisher, R.V. and **Schmincke, H.U.** (1984) *Pyroclastic Rocks*. Springer, Berlin, 472 pp.

Folk, R.L. and **Ward, W.C.** (1957) Brazos river bar: a study in the significant of grain-size parameters. *J. Sedim. Petrol.*, **27,** 3–26.

Francis, P.W., Gardeweg, M., O'Callaghan, L.J., Ramirez, C.F. and **Rothery, D.A.** (1985) Catastrophic debris avalanche deposit of Socompa Volcano, north Chile. *Geology*, **13,** 600–603.

Freundt, A. and **Schmincke, H.U.** (1986) Emplacement of small-volume pyroclastic flows at Laacher See (East Eifel, Germany). *Bull Volcanol.*, **48,** 39–59.

Gomez, C., Lavigne, F., Hadmoko, D.S., Lespinasse, N. and **Wassmer, P.** (2009) Block-and-ash flow deposition: a conceptual model from a GPR survey on pyroclastic-flow deposits at Merapi Volcano, Indonesia. *Geomorphology*, **110,** 118–127.

Hayashi, J.N. and **Self, S.** (1992) A comparison of pyroclastic flow and debris avalanche mobility. *J. Geophys. Res.*, **97,** 9063–9071.

Howard, K.A. (1973) Avalanche mode of motion: implications from lunar examples. *Science*, **180,** 1052–1055.

Inman, D.L. (1952) Measures for describing the size-distribution of sediments. *J. Sedim. Petrol.*, **22,** 125–145.

Iverson, R.M. (1997) The physics of debris flows. *Rev. Geophys.*, **35,** 245–296.

Kamata, K., Kusano, T. and **Yamasaki, K.** (2009) Fractal analysis of fracture strength and energy density of a lava dome based on the grain-size distribution of block-and-ash flows: Unzen Volcano, Japan. *Sediment. Geol.*, **220,** 162–168.

Karatson, D., Sztano, O. and **Telbisz, T.** (2002) Preferred clast orientation in volcaniclastic mass-flow deposits: application of a new photo-statistical method. *J. Sediment. Res.*, **72,** 823–835.

Kelfoun, K., Legros, F. and **Gourgaud, A.** (2000) A statistical study of tree damage by the November 22, 1994 eruption of Merapi volcano (Java, Indonesia): relationships between ash-cloud surges and block-and-ash flows. *J. Volcanol. Geotherm. Res.*, **100,** 379–393.

Le Roux, J.P. (2003) Can dispersive pressure cause inverse grading in grain flows? Discussion. *J. Sedim. Res.*, **73,** 333–334.

Lube, G., Huppert, H.E., Sparks, R.S.J. and **Freundt, A.** (2005) Collapses of two-dimensional granular columns. *Phys. Rev. E*, **72,** 041301.

Lube, G., Cronin, S.J., Platz, T., Freundt, A., Procter, J.N., Henderson, C. and **Sheridan, M.F.** (2007) Flow and deposition of pyroclastic granular flows: a type example from the 1975 Ngauruhoe eruption, New Zealand. *J. Volcanol. Geotherm. Res.*, **161,** 165–186.

Lucchitta, B.K. (1978) A large landslide on Mars. *Geol. Soc. Am. Bull.*, **89,** 1601–1609.

Lucchitta, B.K. (1979) Landslides in Valles Marineris, Mars. *J. Geophys. Res.*, **84,** 8097–8113.

Maria, A. and **Carey, S.** (2007) Quantitative discrimination of magma fragmentation and pyroclastic transport processes using the fractal spectrum technique. *J. Volcanol. Geotherm. Res.*, **161,** 234–246.

McEwen, A.S. and **Malin, M.C.** (1989) Dynamics of Mout St. Helens 1980 pyroclastic flows, rockslide-avalanche, lahars and blast. *J. Volcanol. Geotherm. Res.*, **37,** 205–231.

Middleton, G.V. (1970) Experimental studies related to problems of flysch sedimentation. In: *Flysch Sedimentology in North America* (Ed. J. Lajoie), *Geol. Soc. Can. Spec. Paper*, **7,** 253–272.

Miyabuchi, Y. (1999) Deposits associated with the 1990–1995 eruption of Unzen volcano, Japan. *J. Volcanol. Geotherm. Res.*, **89,** 139–158.

Patra, A.K., Bauer, A.C., Nichita, C.C., Pitman, E.B., Sheridan, M.F., Bursik, M.I., Rupp, B., Webber, A., Stinton, A.J., Namikawa, L.M. and **Renschler, C.S.** (2005) Parallel adaptive simulation of dry avalanches over natural terrain. *J. Volcanol. Geotherm. Res.*, **139,** 1–22.

Ritchie, L.J., Cole, P.D. and **Sparks, R.S.J.** (2002) Sedimentology of deposits from the pyroclastic density current of 26 December (Boxing Day) 1997 at Soufrière Hills Volcano, Montserrat. In: *The Eruption of Soufrière Hills Volcano, Montserrat, from 1995 to 1999* (Eds T.H. Druitt and B.P. Kokelaar), *Geol. Soc. Lond. Mem.*, **21,** 435–456.

Roche, O., Gilbertson, M.A., Phillips, J.C. and **Sparks, R.S.J.** (2004) Experimental study of gas-fluidized granular flows with implications for pyroclastic flow emplacement. *J. Geophys. Res.*, **109,** B10201.

Saucedo, R., Macías, J.L., Bursik, M.I., Mora, J.C., Gavilanes, A. and **Cortes, A.** (2002) Emplacement of pyroclastic flows during the 1998–1999 eruption of Volcan de Colima, Mexico. *J. Volcanol. Geotherm. Res.*, **117,** 129–153.

Saucedo, R., Macías, J.L. and **Bursik, M.I.** (2004) Pyroclastic flow deposits of the 1991 eruption of Volcan de Colima, Mexico. *Bull Volcanol.*, **66,** 291–306.

Savage, S.B. (1979) Gravity flow of cohesionless granular material in chutes and channels. *J. Fluid Mech.*, **92,** 53–96.

Savage, S.B. and **Lun, C.K.K.** (1988) Particle size segregation in inclined chute flow of dry cohesionless granular solids. *J. Fluid Mech.*, **189,** 311–335.

Schumacher, B.A., Shines, K.C., Burton, J.V. and **Papp, M.L.** (1990) A comparison of soil sample homogenization techniques. *Internal Report EPA/600/X-90/043*. US Environmental Protection Agency, Las Vegas, 16 pp.

Schwarzkopf, L.M., Schmincke, H.-U. and **Cronin, S.J.** (2005) A conceptual model for block-and-ash flow basal avalanche transport and deposition, based on deposit architecture of 1998 and 1994 Merapi flows. *J. Volcanol. Geotherm. Res.*, **139,** 117–134.

Siebert, L., Glicken, H. and **Ui, T.** (1987) Volcanic hazards from Bezymianny- and Bandai-type eruptions. *Bull Volcanol.*, **49,** 435–459.

Sohn, Y.K. and **Chough, S.K.** (1989) Depositional processes of the Suwolbong Tuff Ring, Cheju Island (Korea). *Sedimentology*, **36,** 837–855.

Stoopes, G.R. and **Sheridan, M.F.** (1992) Giant debris avalanches from the Colima Volcanic Complex, Mexico: implications for long-runout landslides (>100 km) and hazard assessment. *Geology*, **20,** 299–302.

Sulpizio, R. and **Dellino, P.** (2008) Sedimentology, depositional mechanisms and pulsating behaviour of pyroclastic density currents. In: *Caldera Volcanism: Analysis, Modelling and Response. Developments in Volcanology*, Vol. 10, (Eds J. Gottsman and J. Marti), pp. 58–96. Elsevier, Amsterdam.

Sulpizio, R., Mele, D., Dellino, P. and **La Volpe, L.** (2007) Deposits and physical properties of pyroclastic density currents during complex Subplinian eruptions: the AD 472 (Pollena) eruption of Somma-Vesuvius, Italy. *Sedimentology*, **54,** 607–635.

Takahashi, T. (1981) Debris flow. *Annu. Rev. Fluid Mech.*, **13,** 57–77.

Voight, B. (1978) *Rockslides and Avalanches*. Vol. 1. Elsevier, New York, 833 pp.

Walker, G.P.L. (1971) Grain-size characteristics of pyroclastic deposits. *J. Geol.*, **79,** 696–714.

Walker, G.P.L. (1983) Ignimbrite types and ignimbrite problems. *J. Volcanol. Geotherm. Res.*, **17,** 65–88.

Walter, T.R., Wang, R., Zimmer, M., Grosser, H., Lühr, B. and **Ratdomopurbo, A.** (2007) Volcanic activity influenced by tectonic earthquakes: static and dynamic stress triggering at Mt. Merapi. *Geophys. Res. Lett.*, **34,** L05304, doi: 10.1029/2006GL028710.

Yamamoto, T., Takarada, S. and **Suto, S.** (1993) Pyroclastic flows from the 1991 eruption of Unzen volcano, Japan. *Bull Volcanol.*, **55,** 166–175.

Manuscript received 2 May 2010; accepted 5 January 2011